

# Using Raw and Thermally Modified Fibrous Clay Minerals as Low Concentration $\text{NH}_4^+\text{-N}$ Adsorbents

Christina Vasiliki Lazaratou (✉ [lachrist93@yahoo.gr](mailto:lachrist93@yahoo.gr))

University of Patras: Panepistemio Patron <https://orcid.org/0000-0001-8447-9124>

Irene E. Triantaphyllidou

University of Patras: Panepistemio Patron

Ioannis Pantelidis

University of Patras: Panepistemio Patron

Dimitris A. Chalkias

University of the Peloponnese: Panepistemio Peloponnesou

George Kakogiannis

Geohellas S.A.

Dimitrios V. Vayenas

University of Patras: Panepistemio Patron

Dimitrios Papoulis

University of Patras: Panepistemio Patron

---

## Research Article

**Keywords:** palygorskite, sepiolite, thermal treatment,  $\text{NH}_4^+\text{-N}$ , water treatment, adsorption, ion exchange

**Posted Date:** July 12th, 2021

**DOI:** <https://doi.org/10.21203/rs.3.rs-653532/v1>

**License:**   This work is licensed under a Creative Commons Attribution 4.0 International License.

[Read Full License](#)

---

**Version of Record:** A version of this preprint was published at Environmental Science and Pollution Research on October 21st, 2021. See the published version at <https://doi.org/10.1007/s11356-021-17107-z>.

# 1 Using raw and thermally modified fibrous clay minerals as low concentration $\text{NH}_4^+$ -N adsorbents

2 Christina V. Lazaratou<sup>1\*</sup>, Irene E. Triantaphyllidou<sup>2</sup>, Ioannis Pantelidis<sup>1</sup>, Dimitris A. Chalkias<sup>3</sup>, George  
3 Kakogiannis<sup>4</sup>, Dimitrios V. Vayenas<sup>2,5</sup>, Dimitrios Papoulis<sup>1</sup>

<sup>1\*</sup>Department of Geology, University of Patras, GR-26504 Patras, Greece, [lachristie93@gmail.com](mailto:lchristie93@gmail.com)

<sup>2</sup>Department of Chemical Engineering, University of Patras, GR-26504 Patras, Greece

<sup>3</sup>Nanotechnology & Advanced Materials Laboratory, Department of Electrical and Computer Engineering, University of Peloponnese, GR-26334 Patras, Greece

<sup>4</sup>Geohellas S.A., 8A Pentelis Str., GR-175 64 Athens, Greece

4 <sup>5</sup> Institute of Chemical Engineering Sciences, Foundation for Research and Technology, PO Box 1414, GR-26504,  
5 Patras, Greece

## 6 Abstract

7 Raw and modified fibrous clay minerals palygorskite (Pal) and sepiolite (Sep) were tested for their ability to remove  
8 ammonium from ammonium polluted water. Palygorskite and sepiolite underwent thermal treatment at 400°C (T-Pal and  
9 T-Sep respectively). Raw and thermally treated samples were characterized using XRD, SEM, BET, FT-IR, TGA, zeta  
10 potential and XRF. The techniques verified the effect of thermal treatment on samples structures and the enhancement of  
11 negative charge. Both raw and thermally-activated materials applied in batch kinetic experiments, and found to be  
12 efficient adsorbents in their raw forms, since Pal and Sep achieved 60 and 80%  $\text{NH}_4^+$ -N removal respectively within 20  
13 min of contact for initial  $\text{NH}_4^+$ -N concentration of 4 mg/L. Similar removal rates were gained for other concentrations  
14 representative of contaminated aquifers that were examined, ranging from 1 mg/L to 8 mg/L. Results for the modified T-  
15 Pal and T-Sep minerals showed up to 20% higher removal rate. Saturation tests indicated the positive effect of thermal  
16 treatment on the minerals since T-Pal and T-Sep removal efficiency reached 85% and remained stable for 24 h. However,  
17 competitive ions in real water samples can influence the  $\text{NH}_4^+$ -N removal efficiency of the examined samples. In all  
18 cases, the Freundlich isotherm and pseudo-second kinetic models showed better fitted all examined samples thus  
19 indicating heterogeneous chemisorption.

20 Keywords: palygorskite, sepiolite, thermal treatment,  $\text{NH}_4^+$ -N, water treatment, adsorption, ion exchange

## 21 1. Introduction

22 Ammonium ( $\text{NH}_4^+$ ) is an inorganic pollutant mostly found in wastewater discharges, landfill leachates, industrial sewage  
23 and agricultural areas (Böhlke et al. 2006). It is commonly found in aquifers contaminated from one of the above-  
24 mentioned pollution sources because it is a highly mobile contaminant (Böhlke et al. 2006). Ammonium can be  
25 extremely toxic since it can be transformed into  $\text{NO}_2^-$  or  $\text{NO}_3^-$  via the nitrification process under oxidant conditions and

26 lead to eutrophication in aquatic ecosystems (Rožić 2000). Moreover, when ingested in quantities exceeding 100 mg/kg  
27 of body weight per day, it can cause the formation of ammonium salts, such as ammonium chloride, that are toxic to  
28 human health (WHO 2003). The European Union has set the permitted limit of  $\text{NH}_4^+$  in groundwater as 0.5 mg/L (WHO  
29 2017). In general, the  $\text{NH}_4^+$ -N concentration in aquifers is  $< 0.2$  mg/L, however when anaerobic conditions dominate,  
30 concentrations of 1-5 mg/L can be reached (Voudouris et al. 2013; Rusydi et al. 2020) .

31 A variety of methods has been applied for  $\text{NH}_4^+$  removal from water, such as biological treatment (Yang et al. 2019;  
32 Zeng et al. 2020), air stripping (Gui and Li 2019) and physicochemical techniques, like sorption mechanism (Hou et al.  
33 2016; Vu et al. 2017). Zeolite has been widely used for  $\text{NH}_4^+$  retention since it is a low-cost, widely available and  
34 environmental-friendly material (Fu et al. 2020). Nevertheless, limited research has investigated the efficiency of clay  
35 minerals for  $\text{NH}_4^+$  removal (Alshameri et al. 2018) despite them being as abundant and low-cost as other industrial  
36 minerals.

37 Clay minerals consist of silicon-oxygen tetrahedral and aluminum- oxygen octahedral sheets which are responsible for  
38 their permanent negative charge. The charge is balanced with cationic interlayer counterions which are exchangeable  
39 with other organic or inorganic cations. These counterions are responsible for the minerals high cation exchange capacity  
40 (CEC) (Brigatti et al. 2013). The high CEC and the permanent negative charge that clay minerals present, render them  
41 promising adsorbents for various cationic pollutants (Lazaratou et al. 2020a).

42 Palygorskite (Pal) and sepiolite (Sep) are the only clay minerals classified as belonging to the fibrous group with a  
43 ribbon-like structure (Galán 1996). Both Pal and Sep are 2:1 clay minerals and their special structural characteristics  
44 include high porosity, high specific surface area (SSA) and numerous inner nano-tunnels. Despite the fact that the fibrous  
45 clay minerals present relatively low CEC (Galán 1996), the aforementioned properties ensure both these clay minerals  
46 have high adsorption capacities. Moreover, Pal and Sep deposits exist worldwide, most of which are exploited for a  
47 variety of industrial applications (Murray et al. 2011). Considering that the fibrous clay minerals are used in industry  
48 quite commonly as other clays such as bentonite, their study in environmental applications as adsorbents is crucial, since  
49 could be an alternative and cost-effective choice, especially for the areas that the relative deposits exist (Kastritis et al.  
50 2003; Yenyol 2012).

51 Thermal treatment, or calcination, has been applied to Pal and Sep to improve their adsorption capacities since at  
52 temperatures above 100°C the water in their intercrystalline tunnels is removed causing modifications in their pore  
53 structure and SSA (Chen et al. 2011b). At temperatures of 350-1000°C dehydroxylation takes place, which may reveal  
54 negatively charged sites and result in additional protonated surfaces (Zuo et al. 2017; Lazaratou et al. 2020b). This

55 physical modification outweighs other modification techniques in terms of operational simplicity and cost, as only the  
56 cost entailed is that of energy demand which depends on calcination temperature and time.

57 This study evaluates the effectiveness of raw and thermally-treated palygorskite and sepiolite minerals as cost-effective  
58  $\text{NH}_4^+$ -N adsorbents. Experiments focused on the removal of low concentrations of  $\text{NH}_4^+$ -N that are commonly found in  
59 contaminated aquifers as few studies have concentrated on  $\text{NH}_4^+$ -N removal from groundwater. Moreover, thermal  
60 treatment has not been previously applied to fibrous clay minerals intended for ammonium removal. To determine the  
61 optimum operational conditions, all samples were mineralogically characterized with XRD, SEM, BET,  $\text{N}_2$  sorption -  
62 desorption isotherms, FT-IR, TGA, zeta potential and XRF methods, while batch kinetic experiments were conducted  
63 with varying adsorbent dosages, initial  $\text{NH}_4^+$ -N concentrations, contact time and pH values. Saturation tests were carried  
64 out to examine the potential reusability of the adsorbents. Isotherms and kinetic models were applied to determine the  
65 nature of the adsorption process.

## 66 **2. Materials and Methods**

### 67 **2.1 Samples preparation and thermal treatment**

68 The Pal sample was supplied from Geohellas S.A. (Ventzia basin Grevena, Greece) while Sep was collected from  
69 Solomos village (Korinthos, Greece). The raw samples were washed with distilled water and dried at 40°C for 48 h then  
70 sieved until powder diffraction was obtained (< 50  $\mu\text{m}$ ). For the thermal treatment, 20 g of each powdered sample was  
71 treated at 400°C in a controlled muffled oven for 2 h and then cooled at room temperature in a desiccator. The  
72 temperature of 400°C was selected since it is the minimum where both coordinated water loss and dehydroxylation take  
73 place within the samples, thus, ensuring effective structural changes and cost effectiveness (Perraki and Orfanoudaki  
74 2008; Chen et al. 2011b).

### 75 **2.2 Characterization methods**

76 Before any characterization method, the raw and thermally treated Pal and Sep samples were dried at 50°C for 24 h to  
77 maintain the representative conditions applied to the samples before adsorption batch tests. X-ray diffraction (XRD)  
78 patterns were obtained for the samples in a  $2\theta$  range of 2° to 60° and at a scanning rate of 2°/min, using XRD Bruker D8  
79 advance diffractometer, with Ni-filtered  $\text{CuK}_\alpha$  radiation ( $\lambda = 1.5418 \text{ \AA}$ ). For the semi-quantitative analysis of the clay  
80 minerals composition, the Area method was used according to Bridley and Brown (1980). Their typical morphological  
81 characteristics were verified with scanning electron microscopy (SEM), using a SEM LEO SUPRA 35VP. The  $\text{N}_2$   
82 adsorption-desorption isothermal tests were carried out at 77K on the samples that were previously degassed at 100°C for

83 3 h, using Micromeritics Tristar 3000 analyzer which is equipped with a SmartPrep degasser. From these isotherms, the  
84 Brunauer-Emmet-Teller (BET) surface area, pore size and pore distribution were determined for all the samples.  
85 Fourier-transform infrared spectroscopy (FTIR) spectra were obtained using FT-IR spectrophotometer Spectrum RXI  
86 (Perkin Elmer) at room temperature. The samples were prepared by mixing 0.1 mg of Pal, Sep, T-Pal and T-Sep with  
87 KBr, and then were pressed till pellets were formed. The spectra were collected over 12 scans in the wavenumbers range  
88 from 400  $\text{cm}^{-1}$  to 4000  $\text{cm}^{-1}$ , and were analyzed using Spectrum v5.3.1 software. Thermogravimetric analysis (TGA) was  
89 conducted on a Perkin Elmer Simultaneous Thermal Analyzer STA6000 controlled by Pyris Manager Software, using  
90 nitrogen as a purging gas. For each run, a weighted amount of sample powder ( $\cong 10$  mg) was loaded on a ceramic pan  
91 and heated from 40°C to 600°C, at a heating rate of 10°C/min. Before each measurement, all samples were subjected to  
92 isothermal heating at 40°C for 30 min to eliminate the adsorbed water on their surface from their exposure to ambient  
93 atmosphere, simulating the drying process carried out before each case of their characterization. The X-Ray fluorescence  
94 (XRF) measurements of the major ( $\text{SiO}_2$ ,  $\text{Al}_2\text{O}_3$ ,  $\text{CaO}$ ,  $\text{MgO}$ ,  $\text{MnO}$ ,  $\text{Fe}_2\text{O}_3$ ,  $\text{K}_2\text{O}$ ,  $\text{Na}_2\text{O}$ ,  $\text{P}_2\text{O}_5$ ,  $\text{TiO}_2$ ) elements were  
95 performed. An amount of 1.8 g of dried ground sample was mixed with 0.2 g of wax (acting as a binder) and was pressed  
96 on a base of boric acid to a circular powder pellet of 3.2 cm in diameter. Analyses were performed with a RIGAKU ZSX  
97 PRIMUS II spectrometer, which was equipped with a Rh-anode running at 4kW, for major and trace elements analysis.  
98 The spectrometer was equipped with the diffracting crystals: LIF (200), LIF (220), PET, Ge, RX-25, RX-61, RX-40 and  
99 RX-75. The samples zeta potential was determined by a Zetasizer, Nano ZS (Malvern, UK). For the measurements,  
100 dilute suspensions of various pH values (4-11) and standard ionic strength (0.01M  $\text{KNO}_3$ ) were used. The zeta potential  
101 was reported as the mean of two measurements, and each measurement was the sum of 14 correlograms and fitting  
102 procedures.

### 103 **2.3 Batch kinetic experiments**

104 A series of batch kinetic experiments was conducted for raw Pal, raw Sep, T-Pal, and T-Sep under various adsorbent  
105 dosages (0.4, 0.8, 1.6 and 4.0 g in 200 ml solution), initial  $\text{NH}_4^+$ -N concentrations (1, 2, 4, 6, and 8 mg/L) and pH values  
106 (2, 3, 5, 7, 9 and 11). Solution pH was adjusted using either  $\text{H}_2\text{SO}_4$  or  $\text{NaOH}$  for acidic and basic values, respectively.  
107 The standard  $\text{NH}_4^+$ -N solutions were prepared by dilution of  $\text{NH}_4\text{Cl}$  in deionized water, at standard ionic strength  $I= 0.1$   
108 M using  $\text{KClO}_4$ . The adsorption process was carried out using the jar tester VELP Scientifica JLT6 at 210 rpm. Samples  
109 were collected at different time intervals (2.5, 5, 10, 15, 20, 30 and 40 min) and were centrifuged at 5500 rpm for 3 min.  
110 The supernatant was filtrated through Whatman filters (0.45  $\mu\text{m}$ ) to remove the finest suspended particles. The final  
111 removal efficiency was determined according to Equation 1:

112 
$$R\% = \frac{(C_0 - C_e)}{C_0} \cdot 100 \quad (1)$$

113 where  $C_0$  is the initial  $\text{NH}_4^+\text{-N}$  concentration, and  $C_e$  is the  $\text{NH}_4^+\text{-N}$  concentration after adsorption in equilibrium.

114 **2.4 Saturation test**

115 For the saturation test, the adsorbents were left in contact with 4 mg/L  $\text{NH}_4^+\text{-N}$  for 24 h under constant stirring. Samples  
 116 were then treated as described above and  $\text{NH}_4^+\text{-N}$  was measured according to the analytical methods described in Section  
 117 2.6. The procedure was repeated until each adsorbent was saturated and no further  $\text{NH}_4^+\text{-N}$  could be adsorbed.

118 **2.5 Batch study on a real water system**

119 In these batch series the optimal adsorbents' dosage was applied in 200 ml of University of Patras tap water.  $\text{NH}_4^+\text{-N}$   
 120 concentration was artificially added to the real water sample in accordance with the other batch tests. Samples were then  
 121 treated as described above and  $\text{NH}_4^+\text{-N}$  was measured according to the analytical methods described in Section 2.6. The  
 122 physicochemical characteristics of the water sample are described in Table 1.

123 Table 1. Physicochemical characteristics of University of Patras tap water.

124

125 Physicochemical Characteristics	Tap Water Sample
pH	7.3
126 Electrical Conductivity ( $\mu\text{S/cm}$ )	880
Total Hardness (mg/L, $\text{CaCO}_3$ )	487
127 $\text{Ca}^{+2}$ (mg/L)	159
$\text{Mg}^{+2}$ (mg/L)	22
128 $\text{Na}^+$ (mg/L)	26

129

130 **2.6 Analytical methods**

131  $\text{NH}_4^+\text{-N}$  concentrations were measured using a UV-VIS spectrophotometer Hach Lange DR 5000 at 625 nm according to  
 132 the modified salicylate method (Verdouw et al. 1978). Each sample was reacted with 6% sodium hypochlorite solution  
 133 and salicylate/catalyst solution (sodium salicylate 10%, sodium nitroferricyanide 0.04% and sodium hydroxide 0.5%).  
 134  $\text{NH}_4^+\text{-N}$  concentrations were measured after 10 min color development. All experiments were conducted in duplicate.

## 135 2.7 Isotherm models

136 Data from the adsorption experiments were fitted in Langmuir and Freundlich isotherms to determine adsorbent surface  
137 sites – adsorbate ions relationship (Aydın Temel and Kuleyin 2016) according to the following equations:

$$138 \quad q_e = \frac{(C_0 - C_e)V}{m} \quad (2)$$

139 where  $q_e$  is the amount of exchanged ions (mg /g),  $C_0$  and  $C_e$  are the initial and equilibrium  $\text{NH}_4^+$ -N concentrations in  
140 solution (mg /L), respectively,  $V$  is the solution volume (L),  $m$  is the adsorbent weight (g),

$$141 \quad \frac{C_e}{q_e} = \frac{1}{q_{max}K_L} + \left(\frac{1}{q_{max}}\right)C_e \quad (3)$$

142 where constant  $K_L$  is the  $C_e/q_e$  ratio vs.  $C_e$  variation, where  $q_{max}$  is used, expressing the  $\text{NH}_4^+$ -N maximum uptake. The fit  
143 to the Langmuir isotherm (Equation 3) indicates the nature of the monolayer adsorption (Aydın Temel and Kuleyin  
144 2016).

145 The Freundlich isotherm expresses heterogeneous adsorption surfaces with unequal active sites and energies of  
146 adsorption (Yagub et al. 2014) and can be expressed as:

$$147 \quad \ln q_e = \ln K_F + \frac{1}{n} \ln C_e \quad (4)$$

148 where  $q_e$  is the amount of exchanged ions (mg/g),  $C_e$  is the equilibrium  $\text{NH}_4^+$ -N concentrations in solution (mg /L),  $K_F$  is  
149 the adsorbent capacity, and  $n$  is the Freundlich constant. When  $1/n$  is  $0 < 1/n < 1$  adsorption is considered favorable,  
150 when  $1/n = 1$  adsorption is linear and irreversible, and when  $1/n > 1$  adsorption is a chemical process and unfavorable.  
151 The value of  $1/n < 1$  indicates the adsorption process is physical (Aydın Temel and Kuleyin 2016).

## 152 2.8. Adsorption kinetic models

153 The adsorption rate of  $\text{NH}_4^+$ -N on Pal, Sep, T-Pal and T-Sep can be estimated via kinetic models application, as well as  
154 the optimal adsorption mechanism and adsorbent surficial characteristics can be approached (Karri et al. 2017).  
155 Specifically, the pseudo-first order kinetic model focused on pollutant adsorption mechanisms and the pseudo-second  
156 order kinetic model was applied to predict the chemisorption of  $\text{NH}_4^+$ -N onto the tested adsorbents. The linearized forms  
157 of the kinetic models are expressed by Equations 5 and 6, respectively.

$$158 \quad \ln(q_e - q_t) = \ln q_e - k_1 t \quad (5)$$

$$\frac{t}{q_t} = \frac{1}{k_2 q_e^2} + \frac{1}{q_e} t \quad (6)$$

where  $q_t$  is the amount of adsorbed pollutant at time  $t$  (mg/g), and  $k_1$  (1/min) and  $k_2$  (g/mg min) are the rate constants of  $\text{NH}_4^+$ -N adsorption for the pseudo- first and second order kinetic models, respectively (Karri et al. 2017). The  $k_1$  value can be determined from the slope of the linear plot of  $\ln(q_e - q_t)$  vs  $t$ , and  $k_2$  from the intercept of the linear plot of  $t/q_t$  vs  $t$ . Although both models indicate the adsorption mechanism through time, neither takes into account the diffusion mechanism that can be expressed according to the Weber-Morris model, otherwise known as the intraparticle diffusion model, in Equation 7.

$$q = k_{id} \sqrt{t} + I \quad (7)$$

where  $q$  is the adsorbate amount at time  $t$  and  $k_{id}$  is the intraparticle diffusion constant ( $\text{mg/g min}^{-1/2}$ ). The  $k_{id}$  parameter can be calculated from the slope of the  $q_t$  vs  $t^{0.5}$  linear plot, while  $I$  is the intercept of the vertical axis. If the Weber-Morris plot is linear,  $I=0$  and intraparticle diffusion is the rate limiting step, but when  $I > 0$  two steps take place, firstly the film, followed by the intraparticle diffusion as the rate limiting steps (Svilović et al. 2010).

### 171 3. Results and Discussion

#### 172 3.1. Adsorbent characteristics and proposed $\text{NH}_4^+$ -N removal mechanism

##### 173 3.1.1. XRD

174 The XRD pattern of palygorskite sample (Pal) was characterized by Pal reflections at  $2\theta^\circ$  values  $8.3^\circ$ ,  $20^\circ$ ,  $27^\circ$  and  $34^\circ$ ,  
 175 rendering palygorskite the dominant mineralogical phase (96%) at Pal sample. The  $2\theta^\circ$  reflection at  $6^\circ$  indicated the  
 176 predicted occurrence of saponite as impurity (4%), since this mineral coexists with Pal in the Ventzia basin deposit (Fig.  
 177 1a). Differences were shown at Pal reflections after thermal treatment (T-Pal) (Fig. 1b), where the first characteristic Pal  
 178 reflection intensity at  $8.3^\circ$  was sharply decreased, in contrast to the extended reflection of saponite. Similar results were  
 179 observed by Yan et al. (2012), who recorded a decreased Pal reflection at  $8.3^\circ$ , while a new reflection at  $30^\circ$  was formed  
 180 by dehydration and structural rearrangement. After  $\text{NH}_4^+$ -N adsorption, both Pal (Pal  $\text{NH}_4^+$ -N) and T-Pal (T-Pal  $\text{NH}_4^+$ -N)  
 181 samples preserved the same mineral phases that were described above, since the existed main palygorskite reflections  
 182 and saponite impurity were observed (Fig. 1a,b). However, at Pal  $\text{NH}_4^+$ -N and T-Pal  $\text{NH}_4^+$ -N samples. The reflections  
 183 attributed to palygorskite are decreased, as well as a slight peak shifting was observed at the basal reflections of  $20^\circ$  and  
 184  $35^\circ$  (Fig. 1a,b). The intensity change of the reflections highlights the surficial interaction between adsorbent- adsorbate  
 185 (Papoulis et al. 2019), whereas the peak shifting can be attributed either to the ion exchange that took place or to the

186 surficial bonding that may affect the crystallinity. Moreover, even the small presence of saponite may influence the  
187 surficial interactions with  $\text{NH}_4^+$ , since saponite consists of multiple  $\text{OH}^-$  groups on its surface (Zhou et al. 2019).

188 At the XRD pattern of the sepiolite sample (Sep) the reflections of all other minerals were absent apart from an impurity  
189 of calcite at the reflection at  $30^\circ$  in content of 2% (Fig. 1c). The dominant sepiolite's presence was verified by the typical  
190 Sep reflections at  $7.2^\circ$ ,  $20^\circ$  and  $35^\circ$ , rendering sepiolite the main mineralogical phase (98%). The impact of thermal  
191 treatment (T-Sep) on Sep structure is revealed, since two new reflections appear at  $7.3^\circ$  and  $11.04^\circ$  (Fig. 1d) due to the  
192 formation of sepiolite anhydrite that occurs at temperatures above  $350^\circ\text{C}$  (Perraki and Orfanoudaki 2008). After  $\text{NH}_4^+\text{-N}$   
193 adsorption, Sep (Sep  $\text{NH}_4^+\text{-N}$ ) and T-Sep (T-Sep  $\text{NH}_4^+\text{-N}$ ) samples presented opposed behavior from Pal  $\text{NH}_4^+\text{-N}$  and T-  
194 Pal  $\text{NH}_4^+\text{-N}$  samples, since there was no shifting occurred, while the main reflection at  $7.2^\circ$  in both samples was steeply  
195 increased (Fig. 1c, d). Potentially the Sep and T-Sep purity led to enhanced interactions of the samples pores with  $\text{NH}_4^+$ ,  
196 contributing to the sharply increased reflections (Marler et al. 1996). This verifies the ammonium interaction with the  
197 inside of Sep or T-Sep structure without altering the crystal structure of the samples. Similar behavior was reported in the  
198 study of Alshameri et al. (2018) for vermiculite as ammonium adsorbent.

199

### 200 3.1.2 SEM

201 SEM images revealed the morphology of the Pal and Sep samples before and after thermal treatment. The fibrous  
202 morphology of Pal and Sep were verified (Figs. 2a, 2c respectively), with fiber lengths ranging from 250 nm to 1  $\mu\text{m}$ .  
203 The effect of thermal treatment at  $400^\circ\text{C}$  was significant in both samples (Figs. 2b, d). Specifically, T-Pal fibers (Fig. 2b)  
204 were strongly agglomerated and their length decreased after thermal treatment as a result of the total loss of coordinated  
205 water molecules (Bu et al. 2011; Xavier et al. 2016). T-Sep also presented similar characteristics (Fig. 2d) with shorter  
206 fibers and agglomeration due to the loss of water molecules (Perraki and Orfanoudaki 2008; Miura et al. 2012).

### 207 3.1.3 BET surface area and pore size distribution

208 The  $\text{N}_2$  adsorption-desorption isotherms for raw and thermally-treated clay minerals are presented in Fig. 3. Based on the  
209 IUPAC classification, the isotherms were classified as *Type IV* with  $H_3$ -type hysteresis loop, indicating the dominance of  
210 mesoporosity but also the presence of micropores (Sing et al. 1984). The overlap at  $P/P_0 < 0.4$  verified the microporosity,  
211 while the limited loop at  $0.7 < P/P_0 < 0.9$  is typical of low degree mesoporosity (Cases 1991; Wang et al. 2016), which  
212 may be attributed to aggregates or capillary condensation of typical  $H_3$ -type loop and isotherm *Type IV*, respectively  
213 (Sing et al. 1984). After thermal treatment at  $400^\circ\text{C}$  the loop at  $0.6 < P/P_0 < 0.9$  steepened. This was especially noticeable

214 in T-Sep, since Sep is more fragile than palygorskite due to its Mg-rich composition and the size of its structural  
 215 microchannels (Myriam 1998). Up to 350°C the loss of Sep first coordinated water causes reversible inner channels  
 216 folding, but from 400°C the folding is irreversible, with Sep preserving its structure (Myriam 1998).

217 The SSA values, average pore diameters or widths, and the total pore volumes of the Pal, Sep, T-Sep and T-Pal minerals  
 218 were determined as well (Table 2). The thermally - treated samples showed a > 50% reduction in SSA as the zeolitic  
 219 water and part of the coordinated water or magnesium-coordinated water respectively are removed during treatment  
 220 (Perraki and Orfanoudaki 2008; Chen et al. 2011a). This removal of Mg<sup>+2</sup> within the T-Sep structure may caused the  
 221 reduction in SSA, whereas the increased pore volume could be attributed to this structural rearrangement, as well as the  
 222 secondary occurrence of microporosity resulted from the dehydration of silanol groups which may also explain the more  
 223 intense loop observed after calcination (Balci 1999). In contrast, after calcination at temperatures exceeding 400°C, the  
 224 pore size of T-Pal reduced due to the collapse of Pal nano tunnels and the condensation of silanol groups (Chen et al.  
 225 2011a).

226 Table 2. Specific Surface Area (SSA), average pore diameter and total pore volume of Pal, Sep, T-Pal and T-Sep.

227

Samples	SSA (m <sup>2</sup> /g)	Average pore diameter (nm)	Total pore volume (cm <sup>3</sup> /g)
Pal	221.0	7.2	0.40
Sep	230.0	6.2	0.24
T-Pal	101.9	7.4	0.196
T-Sep	116.7	10.4	0.32

228

### 229 3.1.4 FT-IR

230 The FT-IR spectra of raw and thermally modified Pal and Sep before, and after NH<sub>4</sub><sup>+</sup>-N adsorption can be observed in  
 231 Figs. 4 a-d. Pal sample (Fig. 4a) presented typical bands of Si - O stretching, slightly shifted, at 469 cm<sup>-1</sup>, 1024 cm<sup>-1</sup>,  
 232 1170 cm<sup>-1</sup> and 1655 cm<sup>-1</sup> (Madejová et al. 2017), whereas the band at 1170 cm<sup>-1</sup> can be Si-O bond that connects two  
 233 inverse SiO<sub>4</sub> of palygorskite structure, and the 1200cm<sup>-1</sup> band is typical of the ribbon structure (Blanco et al. 1989; Yan  
 234 et al. 2012). Saponite impurity can be verified based on the band at 650 cm<sup>-1</sup> (Lainé et al. 2017). At the range of 3610 cm<sup>-1</sup>  
 235 <sup>1</sup> to ~ 3200 cm<sup>-1</sup> characteristic bands of OH<sup>-</sup> from zeolitic water groups coordinated with structural Mg are shown (Xavier  
 236 et al. 2016). The FT-IR data verified XRD results that thermal treatment did not influence the mineralogical phase of  
 237 palygorskite, since the same bands with the raw sample are maintained (Fig. 4b). Moreover, the vibration of the band at  
 238 1170 cm<sup>-1</sup> in Fig. 4b is steeply decreased after thermal treatment and a new band at 882 cm<sup>-1</sup> appeared; similarly to the  
 239 observation of Yan et al. (2012) for the analogous band at 1196 cm<sup>-1</sup> and at 885 cm<sup>-1</sup> respectively. Vibration decrease and

240 shifting at  $\sim 3400\text{ cm}^{-1}$  to  $\sim 3600\text{ cm}^{-1}$  that was followed, can be attributed to a partial loss of bound water after the thermal  
241 treatment (Fig. 4b). The total loss of water could be achieved at temperature higher than  $700^\circ\text{C}$  (Xavier et al. 2016). After  
242  $\text{NH}_4^+\text{-N}$  adsorption on Pal (Fig. 4a) an intense band at  $1380\text{ cm}^{-1}$  can be attributed to the newly formed N-H bond,  
243 rendering the ammonium removal on Pal by chemisorption (He et al. 2016).

244 The FT-IR spectra of Sep sample (Fig. 4c) presented bands at  $463\text{ cm}^{-1}$ ,  $683\text{ cm}^{-1}$ ,  $830\text{ cm}^{-1}$ ,  $889\text{ cm}^{-1}$  and  $1020\text{ cm}^{-1}$  that  
245 are referred to Si-O-Si bonds, whereas the bands at  $1659\text{ cm}^{-1}$  and  $3419\text{ cm}^{-1}$  can be attributed to zeolitic water  
246 molecules. In addition, the bands at  $441\text{ cm}^{-1}$  and  $3568\text{ cm}^{-1}$  are representative of Si-O-Mg and surficial Mg-OH bonds of  
247 sepiolite respectively (Perraki and Orfanoudaki 2008). After thermal treatment at  $400^\circ\text{C}$  the Mg- bands are steeply  
248 decreased (Fig. 4d), inducing significant shifting at Si-O-Si band from  $463\text{ cm}^{-1}$  to  $474\text{ cm}^{-1}$ . These results come in  
249 agreement with the BET analysis where Sep structural rearrangement and Mg- removal were referred. After  $\text{NH}_4^+\text{-N}$   
250 adsorption, a slight shifting was observed at the band areas  $1260\text{-}1390\text{ cm}^{-1}$  and  $616\text{ - }730\text{ cm}^{-1}$ , whereas band  
251 differences occurred at the area of  $1380\text{-}1390\text{ cm}^{-1}$ . However, there is not an intense new band; typical of N-H bonding,  
252 because the bands of the sepiolite mineral may overlap these bands. The slight occurred band shifting could be attributed  
253 to interactions taking place on the surface, however, are not as intense as it was observed at Pal and T-Pal samples.

### 254 3.1.5 TGA

255 TGA curves of the raw and thermally treated clay mineral samples are shown in Figure 5. Regarding the raw clay  
256 minerals and, at first, the Pal sample, three distinct weight loss steps can be observed in the TGA curve for the studied  
257 range of temperatures (12% total weight loss). The first step is determined at about  $60^\circ\text{C}$  and has to do with the  
258 elimination of the interparticle adsorbed water, the second step is found at about  $170^\circ\text{C}$  and is assigned to the thermal  
259 dehydration of the sample, while an extra weight loss step appears at a higher temperature region ( $340\text{-}420^\circ\text{C}$ ) (Frost and  
260 Ding 2003). Two considerations can be used for this step according to the literature. The first one is attributed to the  
261 dehydroxylation of the OH units from the octahedral Fe and Al, and the second one (more likely) to irreversible  
262 dehydration of residual bound water. On the other hand, regarding the Sep sample, three weight loss steps may also be  
263 detected for the studied range of temperatures (8% total weight loss). The first step takes place at about  $50^\circ\text{C}$  and is  
264 attributed to the loss of remaining adsorbed water on the sample surface, the second step is determined just above  $240^\circ\text{C}$   
265 and corresponds to the loss of hydration water, while a third step could also be considered at the temperature region  $450\text{-}$   
266  $500^\circ\text{C}$  and has to do with the loss of coordination water (Frost and Ding 2003). Regarding the thermally treated clay  
267 minerals samples, in these cases, the weight loss was found quite reduced compared to the corresponding raw samples  
268 (total weight loss was about 8% for the T-Pal sample and 4% for the T-Sep sample). This was an expected observation

269 since these samples had already undergone a thermal treatment at 400°C. TGA analysis was performed until 600°C and in  
 270 both of the samples the adsorbed water molecules were degraded until 400°C, while a small amount of the structural  
 271 water remained in the samples. The partial loss of adsorbed water at 400°C was also verified at FT-IR spectra.

### 272 3.1.6 Zeta potential

273 The zeta potential distribution (Fig. 6) comes in agreement with previous experimental studies (Alshameri et al. 2018;  
 274 Abrougui et al. 2019). Specifically, the zeta-potential of raw and thermally modified samples was negative at the whole  
 275 pH range examined (4-11). This can be attributed to the isomorphous substitutions of  $Al^{3+}$  or  $Mg^{2+}$  with  $Si^{4+}$  on octahedral  
 276 sheets of minerals, as well as to the potential exchange of monovalent ions with divalent ones, which affect minerals'  
 277 electrochemistry of solid/liquid interface (Alshameri et al. 2018; Abrougui et al. 2019). That resulted in more negatively  
 278 charged interface with pH increase, rendering all of the examined materials be promising adsorbents for cations,  
 279 especially at pH values > 5. Moreover, the thermal treatment had impact on the negative charge of the materials as well,  
 280 since T-Pal and T-Sep samples presented more negative values than the raw samples.

### 281 3.1.7 XRF analysis

282 XRF analysis (Table 3) revealed that the chemical composition of the samples comprises mainly  $SiO_2$  (62-65%) and  
 283  $MgO$  (17-25%), while Pal and T-Pal samples were also rich in Fe (< 9%) due to their deposit lithologies (Kastritis et al.  
 284 2003). The main oxides (Si, Al, Mg and Fe) were observed to remain more-or-less constant following thermal treatment  
 285 although a slight increase was seen in T-Sep and  $SiO_2$  and  $MgO$  decreased slightly in T-Pal. This may be attributed either  
 286 the sample heterogeneity or structural rearrangements that took place after thermal treatment. Oxide percentages  
 287 remained stable after  $NH_4^+$ -N adsorption thus indicating that all the ions present are exchangeable with  $NH_4^+$  without  
 288 strong preferences to one particular ion, verifying that ion exchange is essential mechanism at ammonium removal.  
 289 Moreover, due to the low concentration of  $NH_4^+$ , the potential %mass that could be ion-exchanged may be below the  
 290 detection limits of the XRF equipment.

291 Table 3. Composition of main oxides and loss of ignition (LOI) of Pal, Sep, T-Pal, T-Sep before and after adsorption  
 292 (sample/ $NH_4^+$ ) with XRF analysis.

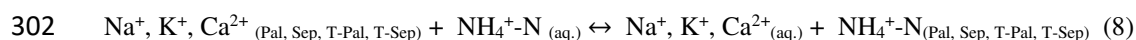
Samples	Main Oxides (% mass)								
	SiO <sub>2</sub>	Al <sub>2</sub> O <sub>3</sub>	MgO	CaO	Na <sub>2</sub> O	K <sub>2</sub> O	MnO	Fe <sub>2</sub> O <sub>3</sub>	LOI
Pal	63.69	1.10	19.78	0.33	0.06	0.04	0.41	9.36	10.00
Sep	63.55	0.11	20.37	0.92	0.06	0.01	0.15	1.09	15.31
T-Pal	62.94	1.10	18.79	0.45	0.07	0.06	0.61	13.35	8.28
T-Sep	64.60	0.23	25.16	2.11	0.07	0.01	0.19	1.55	8.61
Pal/ $NH_4^+$	62.58	1.01	17.86	0.28	0.06	0.04	0.42	9.57	12.35
Sep/ $NH_4^+$	65.18	0.13	24.41	1.61	0.04	0.01	0.15	1.25	11.17

T-Pal /NH <sub>4</sub> <sup>+</sup>	62.16	1.03	17.79	0.50	0.06	0.06	0.60	13.34	7.94
T-Sep /NH <sub>4</sub> <sup>+</sup>	63.34	0.23	24.85	2.07	0.06	0.01	0.19	1.54	9.36

293

294 **3.1.7 Thermal treatment effect and proposed NH<sub>4</sub><sup>+</sup>-N removal mechanism on raw and thermally modified Pal and**  
 295 **Sep**

296 In order to better understand the insight of NH<sub>4</sub><sup>+</sup>-N removal mechanism onto Pal, Sep, T-Pal and T-Sep, the observations  
 297 from characterization methods were evaluated. So far, it was reported that ion exchange between Na<sup>+</sup>, Ca<sup>2+</sup> or K<sup>+</sup> with  
 298 NH<sub>4</sub><sup>+</sup> is the primary mechanism for ammonium removal (He et al. 2016; Alshameri et al. 2018). However, the XRF  
 299 results did not indicate significant reduction at %mass of the exchangeable cations of the adsorbents after NH<sub>4</sub><sup>+</sup>-N  
 300 adsorption (Table 3). This implied either that all the cations are exchangeable with ammonium as expressed in Equation  
 301 8, or that ion exchange partially contributes to ammonium removal on raw and thermally modified fibrous clay minerals.



303 On the other hand, the XRD patterns and FT-IR spectra of Pal and T-Pal verified the surficial interactions of NH<sub>4</sub><sup>+</sup> with  
 304 negatively charged active sites of Pal and T-Pal (Fig. 1,4), because of the decreased intensity of the XRD reflections of  
 305 Pal and T-Pal after NH<sub>4</sub><sup>+</sup>-N adsorption, highlighting the ammonium bonding on the surface. The FT-IR spectra verified  
 306 the results obtained from XRD, since a new band was created at 1380 cm<sup>-1</sup> for the Pal and T-Pal samples after NH<sub>4</sub><sup>+</sup>-N  
 307 adsorption, which is referred to surficial N-H bonding. Moreover, the BET analysis indicated that the SSA of the Pal  
 308 sample was decreased after thermal treatment (T-Pal), nevertheless, according to the zeta potential distribution, T-Pal  
 309 was more negatively charged than Pal at pH range 4-11. Potentially the rearrangement that thermal treatment emerged  
 310 and was observed (Fig. 3), gradually increased the number of exchangeable cations (Chen et al. 2011b), making T-Pal a  
 311 promising adsorbent for cations, such as ammonium, by enhancing its ion exchange capacity in combination with its  
 312 surficial interactions.

313 On the contrary, Sep and T-Sep samples characteristics were differentiated from Pal and T-Pal. Precisely, the XRD  
 314 reflections of Sep and T-Sep samples were increased after NH<sub>4</sub><sup>+</sup>-N adsorption, revealing that potentially the interactions  
 315 between sepiolite samples and ammonium are not mainly surficial. The FT-IR spectra also verified this case, since no  
 316 notable shiftings or new bands occurred after NH<sub>4</sub><sup>+</sup>-N adsorption. Moreover, T-Sep presented an increase in total pore  
 317 volume (0.32 cm<sup>3</sup>/g) and pore diameter (10.4 cm<sup>3</sup>/g) compared to Sep (0.24 and 6.2 cm<sup>3</sup>/g respectively), which can be  
 318 attributed to the inner channels breaking due to the removal of structural Mg. The Mg-O-Si and Mg-OH bonding proved  
 319 to be broken at the FT-IR spectra, as was mentioned in section 3.1.4. All these structural changes in combination with the

320 negative charge at a wide range of pH, render the inner space and surface of Sep playing a key role at  $\text{NH}_4^+$ -N adsorption,  
321 while T-Sep adsorption capacity seems to be enhanced, due to the more negatively charged surface than Sep and the  
322 increase of the pores characteristics as well.

### 323 **3.2. Batch experiments**

#### 324 **3.2.1. Effect of adsorbent dosage and initial concentration**

325 The effect of Pal and Sep dosage on  $\text{NH}_4^+$ -N removal was examined for various initial concentrations of the pollutant. It  
326 was obtained that higher adsorbent dosages lead to higher  $\text{NH}_4^+$ -N removal for all the initial  $\text{NH}_4^+$ -N concentrations  
327 examined for both examined dosages of Pal and Sep (Fig. 7a, b). These results were attributed to the high specific surface  
328 area of both clay minerals which provides numerous, readily-available active sites for  $\text{NH}_4^+$ -N to be adsorbed (Alshameri  
329 et al. 2018). Specifically, the dosage of 4 g Pal or Sep adsorbent in 200 ml solution was found to be the most effective,  
330 especially for the removal of 1 or 2 mg  $\text{NH}_4^+$ -N /L below the permitted limit for drinking water (< 0.5 mg/L). The kinetic  
331 behavior of the highest examined adsorbent dosage (4 g) for all the initial  $\text{NH}_4^+$ -N concentrations examined is shown in  
332 Figure 8.

333 Both Pal and Sep presented maximum  $\text{NH}_4^+$ -N removal efficiencies of 60-80% within the first 20 min for all  $\text{NH}_4^+$ -N  
334 concentrations tested. Specifically, the highest removal efficiency (76%) of Pal was observed for lower initial  $\text{NH}_4^+$ -N  
335 concentrations (1 and 2 mg/L), in contrast with Sep that presented 75-80% removal when  $\text{NH}_4^+$ -N ranged from 4 to 6  
336 mg/L, although its removal capacity decreased for 8 mg  $\text{NH}_4^+$ -N/L. Potentially,  $\text{NH}_4^+$  at low concentrations can contact  
337 with the most of Pal active sites, whereas Pal smaller basal space inhibits the excessed ammonium ions to entry in the  
338 interlayer space, leading to decreased  $\text{NH}_4^+$  -N removal at higher concentrations (Rytwo et al. 2000; Aydın Temel and  
339 Kuleyin 2016). On the other hand, Sep removal efficiency is higher for increased ammonium concentrations for constant  
340 4 g of dosage. This may be attributed to the increased ratio of ammonium ions per L, available to interact with Sep active  
341 sites into the solution, leading to enhanced adsorption capacity. However, since the  $\text{NH}_4^+$  -N removal efficiency of Sep  
342 for 4-6 mg  $\text{NH}_4^+$  -N/L had no significant variation, probably the adsorption capacity of the specific dosage is achieved,  
343 and there were not available active sites to interact with 8 mg  $\text{NH}_4^+$  -N/L.

344 To determine the effect of T-Pal and T-Sep dosage on the removal of  $\text{NH}_4^+$ -N of various concentrations, the batch  
345 experiments were performed by applying the optimum dose of each raw mineral (determined as 4.0 g) for 1, 2, 4, 6 and 8  
346 mg/L  $\text{NH}_4^+$ -N removal. The removal efficiencies of both Pal and Sep increased by 10-20% after thermal treatment, but  
347 also retained the tendency presented as raw materials, concerning the  $\text{NH}_4^+$  -N concentration increase (Fig. 9a, b). The

348 efficiency increase can be attributed to the enhancement of negative charge that thermal treatment emerged according to  
349 the zeta potential results that can be attributed to water loss that alters and possibly slightly increases the interlayer space  
350 of both adsorbents (Zadaka-Amir et al. 2013). Specifically, T-Pal produced 85% removal of 2 mg/L  $\text{NH}_4^+\text{-N}$  compared to  
351 70-75% removal by Pal due to potential ion exchange capacity increase after thermal treatment. The highest removal  
352 efficiencies of T- Sep was observed for 4 and 6 mg/L  $\text{NH}_4^+\text{-N}$  concentrations, since the inner space was increased as the  
353 BET analysis reinsured, whereas thermal treatment did not notably enhance the mineral's removal efficiency for 1 or 2  
354 mg  $\text{NH}_4^+\text{-N/L}$ . It is noteworthy that following thermal treatment, T-Sep was able to successfully lower a 4 mg initial  
355  $\text{NH}_4^+\text{-N/L}$  concentration to below the permitted EU limit. The enhanced removal ability of T-Pal was apparent; however,  
356 final concentrations of ammonium were 0.1 mg/L above the permitted EU limits.

357 Compared to the most frequently used natural adsorbent for  $\text{NH}_4^+\text{-N}$ ; zeolite, the fibrous clay minerals presented close  
358 removal capacity with the study of Fu et al. (2020) or Kotoulas et al. (2019), despite the fact that zeolites decreased the  
359  $\text{NH}_4^+\text{-N}$  below the E.U. limit. Nevertheless, the double adsorbent dosage from current study was used in the study of  
360 Kotoulas et al. (2019), whereas Fu et al. (2020) underwent zeolite two different modification methods for the removal of  
361 5 mg/L  $\text{NH}_4^+\text{-N}$ . Under these conditions, the cost and operational difficulties were higher than the examined conditions  
362 of present study, indicating that the raw and thermally modified fibrous clay minerals can be comparable and competitive  
363 to examined zeolites for water treatment.

### 364 3.2.2. Effect of pH

365 To examine the impact of pH on  $\text{NH}_4^+\text{-N}$  removal, the following conditions were applied: 4 g of adsorbent and 4 mg/L  
366 initial  $\text{NH}_4^+\text{-N}$  concentration were examined with pH values ranging from 2 to 11. These conditions were deemed  
367 suitable as lower ammonium concentrations (1-2 mg/L) are effectively removed to levels below the legislated limit (< 0.5  
368 mg/L), and higher concentrations (6-8 mg/L) remained above this value after adsorption. The experimental results  
369 showed that the removal efficiency of all the adsorbents correlates positively to pH increase (Fig.10), since the  
370 adsorption procedure is enhanced up to the case of pH 9, where it exceeds 85% for the thermally-treated mineral  
371 samples. This efficiency can be explained by the state of  $\text{NH}_4^+$  ions in water as at low pH values they are present in the  
372  $\text{NH}_4^+$  form and at pH values above 8.5 they are present as ammonia ( $\text{NH}_{3(\text{aq})}$ ). At very low pH values, the  $\text{H}^+$  ions compete  
373 strongly with  $\text{NH}_4^+$  for available surface adsorption sites and interactions between adsorbent – adsorbate are inhibited.  
374 Similar results were also recorded by Vu et al. (2017) who used biochar. It is likely that at pH values above 9, most of the  
375  $\text{NH}_4^+$  is transformed to  $\text{NH}_{3(\text{aq})}$  and the electrostatic attraction to clay minerals decreases (Vu et al. 2017; Pan et al. 2019).  
376 The experimental results come in agreement with the zeta potential distribution (Fig. 6). The negatively charged interface

377 at higher pH values, interpreted the low removal efficiency of all the samples at pH range 2-5. Moreover, at pH 6 the zeta  
378 potential decreases more steeply than the lower pH values while at pH 7 and pH 8 the zeta potential remained almost  
379 stable. This may explain the reason why at pH 7 the  $\text{NH}_4^+\text{-N}$  removal efficiency is not the highest, like was noted in the  
380 study of Alhameri et al. (2018), highlighting the samples' origin dependence on interfacial properties. Moreover, despite  
381 the fact at  $\text{pH} > 9$  the zeta potential becomes more negative, is not equalized with enhanced ammonium removal,  
382 potentially due to ammonium alteration to  $\text{NH}_{3(\text{aq})}$  as it was abovementioned.

### 383 3.2.3. Saturation test

384 The potential reusability of Pal, Sep, T-Pal and T-Sep as  $\text{NH}_4^+\text{-N}$  adsorbents was examined using 4 g of each adsorbent, 4  
385 mg/L ammonium solution, and natural pH solution (5.5). The saturation test verified the effects of the thermal treatment  
386 on the fibrous clay minerals (Fig. 11). T-Pal and T-Sep achieved 81% and 85% removal, respectively, within the first 24  
387 h and these rates remained almost constant until the third adsorption cycle (day 3). At 24 h the ammonium removal  
388 efficiency of Pal and Sep samples was already declined. This could be attributed to the fine particle size of the samples in  
389 combination with the limited adsorbent dosage and relatively low ammonium initial concentration. The finest the particle  
390 size is, the sooner desorption rates can be achieved, especially under intense agitation (Keyes and Silcox 1994). Both  
391 untreated minerals achieved 55% removal ( $0.48 \pm 0.05$  mg/g) in 24 h, but only the removal pace of Sep remained almost  
392 stable for two more cycles, whereas Pal adsorption capacity decreased by up to 17% from the second day. According to  
393 this saturation test, T-Pal or T-Sep can be characterized as sufficient adsorbents for groundwater treatment that adsorbed  
394  $0.64 - 0.68 \pm 0.02$  mg/g  $\text{NH}_4^+\text{-N}$  respectively, degrading the  $\text{NH}_4^+\text{-N}$  concentration to the acceptable drinking limits  
395 during 24 h. Nevertheless, none of the raw or thermally-treated clay minerals tested presented sufficient reusability for  
396 treatment of water for  $\text{NH}_4^+\text{-N}$ , but all could be effectively reused for pre-treatment. Pal and Sep both removed  $4.28$   
397  $\pm 0.02$  mg  $\text{NH}_4^+\text{-N/g}$  by the end of the saturation test (day 22), while T-Pal and T-Sep removed  $5.95 \pm 0.04$  mg/g  $\text{NH}_4^+\text{-N}$   
398 in the same period. The multiple adsorption cycles were attributed to the primary saturation of the external surfaces of the  
399 adsorbents. When this point was reached the adsorbate enters into the adsorbent's interlayer space and pores (Alshameri  
400 et al. 2018). No research is available on  $\text{NH}_4^+\text{-N}$  saturation in Pal and Sep to compare the results.

### 401 3.3 Adsorption Isotherms

402 The linear forms of the Langmuir and Freundlich isotherms were applied to Pal, Sep, T-Sep and T-Pal to determine the  
403 variation of their removal capacities with increased  $\text{NH}_4^+\text{-N}$  initial concentrations. Both Langmuir and Freundlich  
404 isotherms presented a good fit to all the adsorbents examined since the  $R^2$  value in all cases is  $> 0.95$  (Table 4).  
405 Nevertheless, the linear form of the Freundlich isotherm expressed better the adsorption of  $\text{NH}_4^+\text{-N}$  on Pal and T-Pal with

406  $R^2$  values of 0.974 and 0.991, respectively, which renders the adsorption a heterogeneous procedure. On the other hand,  
 407 the adsorption behavior of Sep differentiated slightly after thermal treatment as the Langmuir isotherm for Sep presented  
 408 a better fit for  $\text{NH}_4^+\text{-N}$  adsorption, but for T-Sep adsorption is expressed better by the Freundlich isotherm with  $R^2$  0.998  
 409 (compared to  $R^2$  0.991 for the Langmuir isotherm). This result revealed the preference of almost monolayer  $\text{NH}_4^+\text{-N}$   
 410 adsorption on the Sep mineral, which potentially became heterogeneous for T-Sep. This change was probably attributed  
 411 to the increased number micropores occurring after calcination as verified by the BET analysis.

412 Table 4. Comparison of adsorption isotherms constants for Pal, Sep, T-Pal, T-Sep.

	Langmuir isotherm				Freundlich isotherm				
	Pal	Sep	T-Pal	T-Sep	Pal	Sep	T-Pal	T-Sep	
$q_{max}$ (mg/g)	0.38	0.31	0.44	0.93	$1/n$	0.839	0.642	0.6697	0.8750
$K_L$	0.353	0.901	0.657	0.144	$K_F$	0.099	0.125	0.1592	0.1132
$R^2$	0.952	0.993	0.954	0.991	$R^2$	0.974	0.954	0.991	0.998

413

#### 414 3.4 Adsorption kinetic models

415 The relative parameters of all applied kinetic models (pseudo-first order, pseudo-second order and intra particle  
 416 diffusion) are presented in Table 5. The correlation coefficients ( $R^2 > 0.99$ ) showed that the pseudo-second order fit the  
 417 data better than the other two models. These results were in agreement with FT-IR spectra and other studies that  
 418 examined  $\text{NH}_4^+\text{-N}$  removal from aqueous solutions using aluminosilicate adsorbents and concluded chemisorption as  
 419 adequately expressing  $\text{NH}_4^+\text{-N}$  removal on clay minerals (Sun et al. 2017; Alshameri et al. 2018). Adsorption capacity at  
 420 equilibrium ( $q_e$ ) is a significant parameter of each model's evaluation. From each kinetic model result a  $q_{ecal}$  value, is  
 421 determined from the intercept and the slope of the pseudo-first and pseudo-second order plots, respectively, is further  
 422 compared to the maximum removal rate at equilibrium ( $q_{exp}$ ). In all cases, the  $q_{exp}$  variables were in full agreement with  
 423 the  $q_{ecal}$  from the pseudo-second order model, compare to pseudo - first order  $q_{ecal}$  (Table 5), rendering the pseudo -  
 424 second order the appropriate kinetic mechanism for  $\text{NH}_4^+\text{-N}$  adsorption on the studied adsorbents.

425 The Weber-Morris model is parted from two linear segments (Table 5). In the first stage  $\text{NH}_4^+\text{-N}$  diffuses from the  
 426 aqueous solution to liquid:solid interface, while in the second stage the adsorbate diffuses from the interface into the  
 427 adsorbent pores Weber and Morris (1963). In all cases, Stage 1  $k_{id} >$  Stage 2  $k_{id}$ , thus indicating the rapid diffusion of  
 428  $\text{NH}_4^+\text{-N}$  at the solids interface, compared to a very slow rate diffusion in their inner pores (Genethliou et al. 2021).

429 Table 5. Kinetic parameters of pseudo-first order, pseudo- second order and intraparticle diffusion kinetic models for  
 430  $\text{NH}_4^+$ -N adsorption from Pal, Sep, T-Pal and T-Sep.

	Pseudo-first order				Pseudo-second order				Weber Morris model			
	$q_{exp}$ (mg/g)	$q_{ecal}$ (mg/g)	$k_1$	$R^2$	$q_{ecal}$ (mg/g)	$h$	$k_2$	$R^2$		$k_{id}$	$R^2$	$I$
<b>Pal</b>	0.138	0.043	0.128	0.832	0.138	0.055	2.80	0.992	Stage 1	0.033	0.589	0.089
									Stage 2	0.0075	0.992	
<b>Sep</b>	0.147	0.05	0.121	0.672	0.147	0.379	18.27	0.993	Stage 1	0.0048	0.896	0.027
									Stage 2	0.0003	0.6075	
<b>T-Pal</b>	0.145	0.052	0.078	0.603	0.145	0.327	47.25	0.999	Stage 1	0.0197	0.991	0.162
									Stage 2	0.0058	0.982	
<b>T-Sep</b>	0.146	0.061	0.086	0.986	0.146	0.489	21.42	0.999	Stage 1	0.0103	0.865	0.02
									Stage 2	0.0042	0.905	

431

### 432 3.5 Real-water application of the adsorbents

433 The raw and thermally treated samples were applied in the optimal dosage determined at the previous batch experiments  
 434 (4 g adsorbent), for 4 mg/L  $\text{NH}_4^+$ -N degradation from ammonium rich tap water. According to Table 1, the water  
 435 consistency is enriched in potentially competitive cations for  $\text{NH}_4^+$ , such as  $\text{Na}^+$ ,  $\text{Ca}^{2+}$  and  $\text{Mg}^{2+}$ , as well as is extremely  
 436 hard water (WHO, 2011). Under these conditions, Pal and T-Pal removal efficiency for  $\text{NH}_4^+$ -N was strongly influenced,  
 437 since it was decreased up to 50% for both of the samples (Fig. 12). Palygorskite clay mineral has reported in other studies  
 438 strong ion exchange affinity for  $\text{Ca}^{2+}$  spontaneously (Lazaratou et al. 2020a), which can be inhibiting factor for  
 439 ammonium removal (Yin and Kong 2014). Sep and T-Sep samples' removal efficiency for  $\text{NH}_4^+$ -N was impacted as  
 440 well; however, 25% and 20% decrease was noted (Fig.10), rendering Sep and T-Sep with stronger affinity for ammonium  
 441 than Pal and T-Pal samples. Despite the decline at  $\text{NH}_4^+$ -N removal capacity of the examined samples, further  
 442 investigation must be conducted, since there is limited literature about natural water systems and how their composition,  
 443 or the concentration of the existed ionic species influence interactions between ammonium and clay minerals' interface.

### 444 4. Conclusions

445 Raw and thermally-treated palygorskite (Pal / T-Pal) and sepiolite (Sep / T-Sep) were applied as low concentration  $\text{NH}_4^+$ -  
 446 N adsorbents from aqueous solutions. The extensive characterization of the samples verified the thermal treatment effect  
 447 and the expected structural rearrangements. Pal, Sep, T-Pal and T-Sep presented different adsorptive properties,  
 448 especially after thermal treatment, since Pal and T-Pal mostly interact with  $\text{NH}_4^+$ -N on its surface, conversely to Sep and  
 449 T-Sep where the inner interactions are dominant. According to a series of batch kinetic experiments,  $\text{NH}_4^+$ -N removal  
 450 process was quite rapid and preferable at pH 4-9. Removal rates were adequate to reduce  $\text{NH}_4^+$ -N concentrations to

451 below the permitted EU limit for drinking water for initial  $\text{NH}_4^+\text{-N}$  concentrations of 1 and 2 mg/L, thus rendering Pal,  
452 Sep, T-Pal and T-Sep suitable materials for the treatment of most contaminated aquifers. T-Sep can also be used to treat  
453 groundwaters with initial  $\text{NH}_4^+\text{-N}$  concentration of 4 mg/L. Nevertheless, the presence of competitive ions such as  $\text{Ca}^{2+}$   
454 strongly deteriorate ammonium interaction with Pal and T-Pal, indicating that its application in very hard waters may  
455 prohibit  $\text{NH}_4^+\text{-N}$  degradation. On the contrary, Sep and T-Sep may not be strongly influenced from competitive ions  
456 presentation, but achieved decreased  $\text{NH}_4^+\text{-N}$  removal up to 25%.

457 The saturation test indicated that T-Pal and T-Sep are effective at  $\text{NH}_4^+\text{-N}$  removal for 24 h but cannot be reused for  
458 water treatment when solutions are highly contaminated (4 mg  $\text{NH}_4^+\text{-N/L}$ ). Nevertheless, Pal, Sep, T-Pal and T-Sep can  
459 be applied as suitable pre-treatment materials for multiple times. Mechanical and kinetic properties of the procedure were  
460 determined using the linear forms of Langmuir and Freundlich isotherm models, as well as the linear form of pseudo-  
461 first, pseudo-second order and Weber-Morris kinetic models. All the above-mentioned models fit to the data of each  
462 tested mineral sample, however, the Freundlich isotherm and pseudo-second kinetic models presented better fits for all  
463 samples, thus indicating the heterogeneous nature of adsorption via strong chemical bonds (chemisorption).

#### 464 **Acknowledgements**

465 This research did not receive any specific grant from funding agencies in the public, commercial, or not-for-profit  
466 sectors. The authors would like to thank Dr. Paraskevi Lampropoulou from University of Patras for XRD analysis, Dr.  
467 Vayia Xanthopoulou from the Laboratory of Electron Microscopy and Microanalysis at University of Patras for the XRF  
468 analysis and Dr. C. Anastasopoulos from Advanced Polymers & Hybrid Nanomaterials Research Laboratory of  
469 Chemistry Department at University of Patras for FT-IR samples preparation. Also, the authors acknowledge Dr.  
470 Vassilios Dracopoulos from FORTH, Patras for the SEM images analysis.

#### 471 **Authors' contributions**

472 Christina V. Lazaratou: Investigation, Methodology, Visualization, Writing-original draft Irene E. Triantaphyllidou:  
473 Methodology, Visualization, Writing- Reviewing and editing Ioannis Pantelidis: Methodology, Visualization Dimitrios  
474 A. Chalkias: Methodology, Writing-original draft George Kakogiannis: Resources Dimitrios V. Vayenas:  
475 Conceptualization, Resources, Project administration, Writing- Reviewing and editing Dimitrios Papoulis:  
476 Conceptualization, Resources, Supervision

477 **Data availability:** The datasets used and/or analyzed during the current study are available from the corresponding  
478 author on reasonable request.

479 **Funding:** Not applicable

480 **Declarations**

481 Ethics approval and consent to participate: Not applicable

482 Consent for publication: Not applicable

483 Competing interests: The authors declare no competing interests.

484 **References**

485 Abrougui MM, Lopez-Lopez MT, Duran JDG (2019) Mechanical properties of magnetic gels containing rod-like  
486 composite particles. *Phil Trans R Soc A* 377:20180218. <https://doi.org/10.1098/rsta.2018.0218>

487 Alshameri A, He H, Zhu J, et al (2018) Adsorption of ammonium by different natural clay minerals:  
488 Characterization, kinetics and adsorption isotherms. *Applied Clay Science* 159:83–93.  
489 <https://doi.org/10.1016/j.clay.2017.11.007>

490 Aydın Temel F, Kuleyin A (2016) Ammonium removal from landfill leachate using natural zeolite: kinetic,  
491 equilibrium, and thermodynamic studies. *Desalination and Water Treatment* 57:23873–23892.  
492 <https://doi.org/10.1080/19443994.2015.1136964>

493 Balci S (1999) Effect of heating and acid pre-treatment on pore size distribution of sepiolite. *Clay Minerals* 34:647–  
494 655

495 Blanco C, González F, Pesquera C, et al (1989) Differences Between One Aluminic Palygorskite and Another  
496 Magnesian by Infrared Spectroscopy. *Spectroscopy Letters* 22:659–673. <https://doi.org/10.1080/00387018908053926>

497 Böhlke JK, Smith RL, Miller DN (2006) Ammonium transport and reaction in contaminated groundwater:  
498 Application of isotope tracers and isotope fractionation studies: NH<sub>4</sub><sup>+</sup> TRANSPORT IN CONTAMINATED  
499 GROUNDWATER. *Water Resour Res* 42:. <https://doi.org/10.1029/2005WR004349>

500 Brigatti, M.F., Galán, E., Theng, B.K.G., 2013. Structure and mineralogy of clay minerals. In: Bergaya, F., Lagaly,  
501 G. (Eds.), *Handbook of Clay Science*. Vol. 5. Elsevier, pp.21–81 (Chapter 2).

502

503 Brindley GW, Brown G (1980) X-ray diffraction procedures for clay mineral identification. In *Crystal Structures of*  
504 *Clay Minerals and Their X-ray Identification*; Brindley, G.W., Brown, G., Eds.; Miner. Soc.: London, UK, pp. 305–  
505 356.

506 Bu X, Zhang G, Guo Y (2011) Thermal modified palygorskite: Preparation, characterization, and application for  
507 cationic dye-containing wastewater purification. *Desalination and Water Treatment* 30:339–347.  
508 <https://doi.org/10.5004/dwt.2011.2242>

509 Cases JM (1991) Evolution of the Porous Structure and Surface Area of Palygorskite Under Vacuum Thermal  
510 Treatment. *Clays and Clay Minerals* 39:191–201. <https://doi.org/10.1346/CCMN.1991.0390211>

511 Chen H, Zhao J, Zhong A, Jin Y (2011a) Removal capacity and adsorption mechanism of heat-treated palygorskite  
512 clay for methylene blue. *Chemical Engineering Journal* 174:143–150. <https://doi.org/10.1016/j.cej.2011.08.062>

513 Chen T, Liu H, Li J, et al (2011b) Effect of thermal treatment on adsorption–desorption of ammonia and sulfur  
514 dioxide on palygorskite: Change of surface acid–alkali properties. *Chemical Engineering Journal* 166:1017–1021.  
515 <https://doi.org/10.1016/j.cej.2010.11.094>

516 Frost RL, Ding Z (2003) Controlled rate thermal analysis and differential scanning calorimetry of sepiolites and  
517 palygorskites. *Thermochimica Acta* 397:119–128. [https://doi.org/10.1016/S0040-6031\(02\)00228-9](https://doi.org/10.1016/S0040-6031(02)00228-9)

518 Fu H, Li Y, Yu Z, et al (2020) Ammonium removal using a calcined natural zeolite modified with sodium nitrate.  
519 *Journal of Hazardous Materials* 393:122481. <https://doi.org/10.1016/j.jhazmat.2020.122481>

520 Galan E (1996) Properties and applications of palygorskite-sepiolite clays. *Clay miner* 31:443–453.  
521 <https://doi.org/10.1180/claymin.1996.031.4.01>

522 Genethliou C, Triantaphyllidou IE, Giannakis D, et al (2021) Simultaneous removal of ammonium nitrogen,  
523 dissolved chemical oxygen demand and color from sanitary landfill leachate using natural zeolite. *Journal of*  
524 *Hazardous Materials* 406:124679. <https://doi.org/10.1016/j.jhazmat.2020.124679>

525 Gui H, Li X (2019) Removing ammonia from skim by air stripping with rotating packed bed. *Chinese Journal of*  
526 *Chemical Engineering* 27:528–533. <https://doi.org/10.1016/j.cjche.2018.06.027>

527 He Y, Lin H, Dong Y, et al (2016) Simultaneous removal of ammonium and phosphate by alkaline-activated and  
528 lanthanum-impregnated zeolite. *Chemosphere* 164:387–395. <https://doi.org/10.1016/j.chemosphere.2016.08.110>

529 Hou J, Huang L, Yang Z, et al (2016) Adsorption of ammonium on biochar prepared from giant reed. *Environ Sci*  
530 *Pollut Res* 23:19107–19115. <https://doi.org/10.1007/s11356-016-7084-4>

531 Karri RR, Jayakumar NS, Sahu JN (2017) Modelling of fluidised-bed reactor by differential evolution optimization  
532 for phenol removal using coconut shells based activated carbon. *Journal of Molecular Liquids* 231:249–262.  
533 <https://doi.org/10.1016/j.molliq.2017.02.003>

534 Kastritis ID, Kacandes GH, Mposkos E (2003) The palygorskite and Mg-Fe-smectite clay deposits of the Ventzia  
535 basin, western Macedonia, Greece. *Mineral exploration and Sustainable Development* 4

536 Keyes BR, Silcox GD (1994) Fundamental Study of the Thermal Desorption of Toluene from Montmorillonite Clay  
537 Particles. *Environ Sci Technol* 28:840–849. <https://doi.org/10.1021/es00054a015>

538 Kotoulas A, Agathou D, Triantaphyllidou I, et al (2019) Zeolite as a Potential Medium for Ammonium Recovery  
539 and Second Cheese Whey Treatment. *Water* 11:136. <https://doi.org/10.3390/w11010136>

540 Lainé M, Balan E, Allard T, et al (2017) Reaction mechanisms in swelling clays under ionizing radiation: influence  
541 of the water amount and of the nature of the clay mineral. *RSC Adv* 7:526–534.  
542 <https://doi.org/10.1039/C6RA24861F>

543 Lazaratou CV, Panagiotaras D, Panagopoulos G, et al (2020a) Ca treated Palygorskite and Halloysite clay minerals  
544 for Ferrous Iron (Fe + 2 ) removal from water systems. *Environmental Technology & Innovation* 19:100961.  
545 <https://doi.org/10.1016/j.eti.2020.100961>

546 Lazaratou CV, Vayenas DV, Papoulis D (2020b) The role of clays, clay minerals and clay-based materials for nitrate  
547 removal from water systems: A review. *Applied Clay Science* 185:105377.  
548 <https://doi.org/10.1016/j.clay.2019.105377>

549 Madejová, J., Gates, W.P., Petit, S., 2017. Infrared and Raman spectroscopies of Clay Minerals. In: Gates, W.P,  
550 Klopogge, J.T., Madejova, J., Bergaya, F. (Eds.), *Developments in Clay Science Volume 8*. Elsevier, pp. 143–149

551 Marler B, Oberhagemann U, Vortmann S, Gies H (1996) Influence of the sorbate type on the XRD peak intensities  
552 of loaded MCM-41. *Microporous Materials* 6:375–383. [https://doi.org/10.1016/0927-6513\(96\)00016-8](https://doi.org/10.1016/0927-6513(96)00016-8)

553 Miura A, Nakazawa K, Takei T, et al (2012) Acid-, base-, and heat-induced degradation behavior of Chinese  
554 sepiolite. *Ceramics International* 38:4677–4684. <https://doi.org/10.1016/j.ceramint.2012.02.050>

555 Murray HH, Pozo M, Galán E (2011) An Introduction to Palygorskite and Sepiolite Deposits—Location, Geology  
556 and Uses. In: *Developments in Clay Science*. Elsevier, pp 85–99

557 Myriam M (1998) Structural and Textural Modifications of Palygorskite and Sepiolite under Acid Treatment. *Clays  
558 and Clay Minerals* 46:225–231. <https://doi.org/10.1346/CCMN.1998.0460301>

559 Pan M, Zhang M, Zou X, et al (2019) The investigation into the adsorption removal of ammonium by natural and  
560 modified zeolites: kinetics, isotherms, and thermodynamics. *WSA* 45:.  
561 <https://doi.org/10.17159/wsa/2019.v45.i4.7546>

562 Papoulis D, Somalakidi K, Todorova N, et al (2019) Sepiolite/TiO<sub>2</sub> and metal ion modified sepiolite/TiO<sub>2</sub>  
563 nanocomposites: synthesis, characterization and photocatalytic activity in abatement of NO<sub>x</sub> gases. *Applied Clay  
564 Science* 179:105156. <https://doi.org/10.1016/j.clay.2019.105156>

565 Perraki Th, Orfanoudaki A (2008) Study of raw and thermally treated sepiolite from the Mantoudi area, Euboea,  
566 Greece: X-ray diffraction, TG/DTG/DTA and FTIR investigations. *J Therm Anal Calorim* 91:589–593.  
567 <https://doi.org/10.1007/s10973-007-8329-8>

568 Rozic M (2000) Ammoniacal nitrogen removal from water by treatment with clays and zeolites. *Water Research*  
569 34:3675–3681. [https://doi.org/10.1016/S0043-1354\(00\)00113-5](https://doi.org/10.1016/S0043-1354(00)00113-5)

570 Rusydi AF, Onodera S-I, Saito M, et al (2020) Potential Sources of Ammonium-Nitrogen in the Coastal  
571 Groundwater Determined from a Combined Analysis of Nitrogen Isotope, Biological and Geological Parameters,  
572 and Land Use. *Water* 13:25. <https://doi.org/10.3390/w13010025>

573 Rytwo G, Nir S, Crespin M, Margulies L (2000) Adsorption and Interactions of Methyl Green with Montmorillonite  
574 and Sepiolite. *Journal of Colloid and Interface Science* 222:12–19. <https://doi.org/10.1006/jcis.1999.6595>

575 Sing KSW, Everett DH, Haul RAW, et al (1984) REPORTING PHYSISORPTION DATA FOR GAS/SOLID  
576 SYSTEMS with Special Reference to the Determination of Surface Area and Porosity. Pure and Applied Chemistry  
577 57:603–619

578 Sun N, Shi W, Ma L, Yu S (2017) Investigations on the mechanism, kinetics and isotherms of ammonium and humic  
579 acid co-adsorption at low temperature by 4A-molecular sieves modified from attapulgite. RSC Adv 7:17095–17106.  
580 <https://doi.org/10.1039/C7RA00268H>

581 Svilović S, Rušić D, Bašić A (2010) Investigations of different kinetic models of copper ions sorption on zeolite  
582 13X. Desalination 259:71–75. <https://doi.org/10.1016/j.desal.2010.04.033>

583 Verdouw, H, van Echteld, CJA, Dekkers, EMJ, (1978) Ammonia determination based on indophenol formation with  
584 sodium salicylate. Water Res. 12, 399–402. [https://doi.org/10.1016/0043-1354\(78\)90107-0](https://doi.org/10.1016/0043-1354(78)90107-0).

585 Voudouris K, Panagopoulos A, Koumantakis I (2013) Nitrate pollution in the coastal aquifer system of the  
586 Korinthos Prefecture (Greece). Global NEST Journal 6:31–38. <https://doi.org/10.30955/gnj.000236>

587 Vu TM, Trinh VT, Doan DP, et al (2017) Removing ammonium from water using modified corncob-biochar.  
588 Science of The Total Environment 579:612–619. <https://doi.org/10.1016/j.scitotenv.2016.11.050>

589 Wang W, Tian G, Wang D, et al (2016) All-into-one strategy to synthesize mesoporous hybrid silicate microspheres  
590 from naturally rich red palygorskite clay as high-efficient adsorbents. Sci Rep 6:39599.  
591 <https://doi.org/10.1038/srep39599>

592 Weber, W.J., Morris, J.C., 1963. Kinetics of adsorption on carbon from solution. J. Sanit. Eng. Div. 89, 31–60

593 World Health Organization (WHO), 2003. Ammonia in Drinking-water. Heal San Fr 2,  
594 [http://www.who.int/water\\_sanitation\\_health/dwq/che](http://www.who.int/water_sanitation_health/dwq/che).

595 World Health Organization (WHO), 2011. Hardness in Drinking water,  
596 [https://www.who.int/water\\_sanitation\\_health/dwq/chemicals/hardness.pdf](https://www.who.int/water_sanitation_health/dwq/chemicals/hardness.pdf) (accessed 31/3/ 21)

597 World Health Organization, 2017. Drinking Water Parameter Cooperation Project. Support to the revision of Annex  
598 I Council Directive 98/83/EC on the Quality of Water Intended for Human Consumption (Drinking Water Directive)  
599 Recommendations, 1–240.

600 Xavier KCM, Santos MSF, Osajima JA, et al (2016) Thermally activated palygorskites as agents to clarify soybean  
601 oil. *Applied Clay Science* 119:338–347. <https://doi.org/10.1016/j.clay.2015.10.037>

602 Yagub MT, Sen TK, Afroze S, Ang HM (2014) Dye and its removal from aqueous solution by adsorption: A review.  
603 *Advances in Colloid and Interface Science* 209:172–184. <https://doi.org/10.1016/j.cis.2014.04.002>

604 Yan W, Liu D, Tan D, et al (2012) FTIR spectroscopy study of the structure changes of palygorskite under heating.  
605 *Spectrochimica Acta Part A: Molecular and Biomolecular Spectroscopy* 97:1052–1057.  
606 <https://doi.org/10.1016/j.saa.2012.07.085>

607 Yang J-R, Wang Y, Chen H, Lyu Y-K (2019) Ammonium removal characteristics of an acid-resistant bacterium  
608 *Acinetobacter* sp. JR1 from pharmaceutical wastewater capable of heterotrophic nitrification-aerobic denitrification.  
609 *Bioresource Technology* 274:56–64. <https://doi.org/10.1016/j.biortech.2018.10.052>

610 Yenyol M (2012) Geology and mineralogy of a sepiolite-palygorskite occurrence from SW Eskişehir (Turkey). *Clay  
611 miner* 47:93–104. <https://doi.org/10.1180/claymin.2012.047.1.93>

612 Yin H, Kong M (2014) Simultaneous removal of ammonium and phosphate from eutrophic waters using natural  
613 calcium-rich attapulgite-based versatile adsorbent. *Desalination* 351:128–137.  
614 <https://doi.org/10.1016/j.desal.2014.07.029>

615 Zadaka-Amir D, Bleiman N, Mishael YG (2013) Sepiolite as an effective natural porous adsorbent for surface oil-  
616 spill. *Microporous and Mesoporous Materials* 169:153–159. <https://doi.org/10.1016/j.micromeso.2012.11.002>

617 Zeng J, Chabi K, Hu Y, et al (2020) Ammonium removal of biological roughing filter for rural drinking water  
618 pretreatment. *Water Supply* 20:2768–2778. <https://doi.org/10.2166/ws.2020.171>

619 Zhou CH, Zhou Q, Wu QQ, et al (2019) Modification, hybridization and applications of saponite: An overview.  
620 *Applied Clay Science* 168:136–154. <https://doi.org/10.1016/j.clay.2018.11.002>

621 Zuo Q, Gao X, Yang J, et al (2017) Investigation on the thermal activation of montmorillonite and its application for  
622 the removal of U(VI) in aqueous solution. *Journal of the Taiwan Institute of Chemical Engineers* 80:754–760.  
623 <https://doi.org/10.1016/j.jtice.2017.09.016>

624

625 **Figure captions**

626 Figure 1. XRD patterns of a) Pal b) T –Pal c) Sep and d) T-Sep before and after  $\text{NH}_4^+\text{-N}$  adsorption where P:  
627 palygorskite, S: saponite, Sep: sepiolite, AnSep: sepiolite anhydrite and C: calcite.

628 Figure 2. Scanning Electron Microscopy (SEM) images of a) Pal b) Sep c) T-Pal and d) T-Sep at 200 nm.

629 Figure 3.  $\text{N}_2$  sorption – desorption isotherms plot from BET analysis for Pal, Sep, T-Pal and T-Sep.

630 Figure 4. FT-IR spectra before and after  $\text{NH}_4^+\text{-N}$  adsorption of a) Pal b) T-Pal c) Sep and d) T-Sep.

631 Figure 5. TGA curves of Pal, Sep, T-Pal and T-Sep.

632 Figure 6. The zeta potential of Pal, Sep, T-Pal and T-Sep at pH range 4-11.

633 Figure 7. Maximum  $\text{NH}_4^+\text{-N}$  Removal Efficiency (%) with 0.4, 0.8, 1.6 and 4 g a)Pal and b)Sep for  $\text{NH}_4^+\text{-N}$   
634 initial concentration 1, 2, 4, 6 and 8 mg/L. The removal efficiency (%) is the mean value from duplicate  
635 experiments.

636 Figure 8. The effect of initial concentration on  $\text{NH}_4^+\text{-N}$  removal by 4 g a) Pal and b) Sep.

637 Figure 9. The effect of initial concentration on  $\text{NH}_4^+\text{-N}$  removal by 4 g a) T- Pal and b) T-Sep.

638 Figure 10. The effect of pH on  $\text{NH}_4^+\text{-N}$  removal by 4 g Pal, Sep, T- Pal and T-Sep. (4 mg  $\text{NH}_4^+\text{-N}$  /L, V= 200  
639 ml, 20 min)

640 Figure 11. Saturation test of 4 g Pal, Sep, T-Pal and T-Sep in  $\text{NH}_4^+\text{-N}$  solution. (4 mg  $\text{NH}_4^+\text{-N}$  /L, V= 200 ml,  
641 pH= 5.5)

642 Figure 12. Removal efficiency (%) of 4 g Pal, Sep, T-Pal and T-Sep in real water sample contaminated with 4  
643 mg/L  $\text{NH}_4^+\text{-N}$ .

644

# Figures

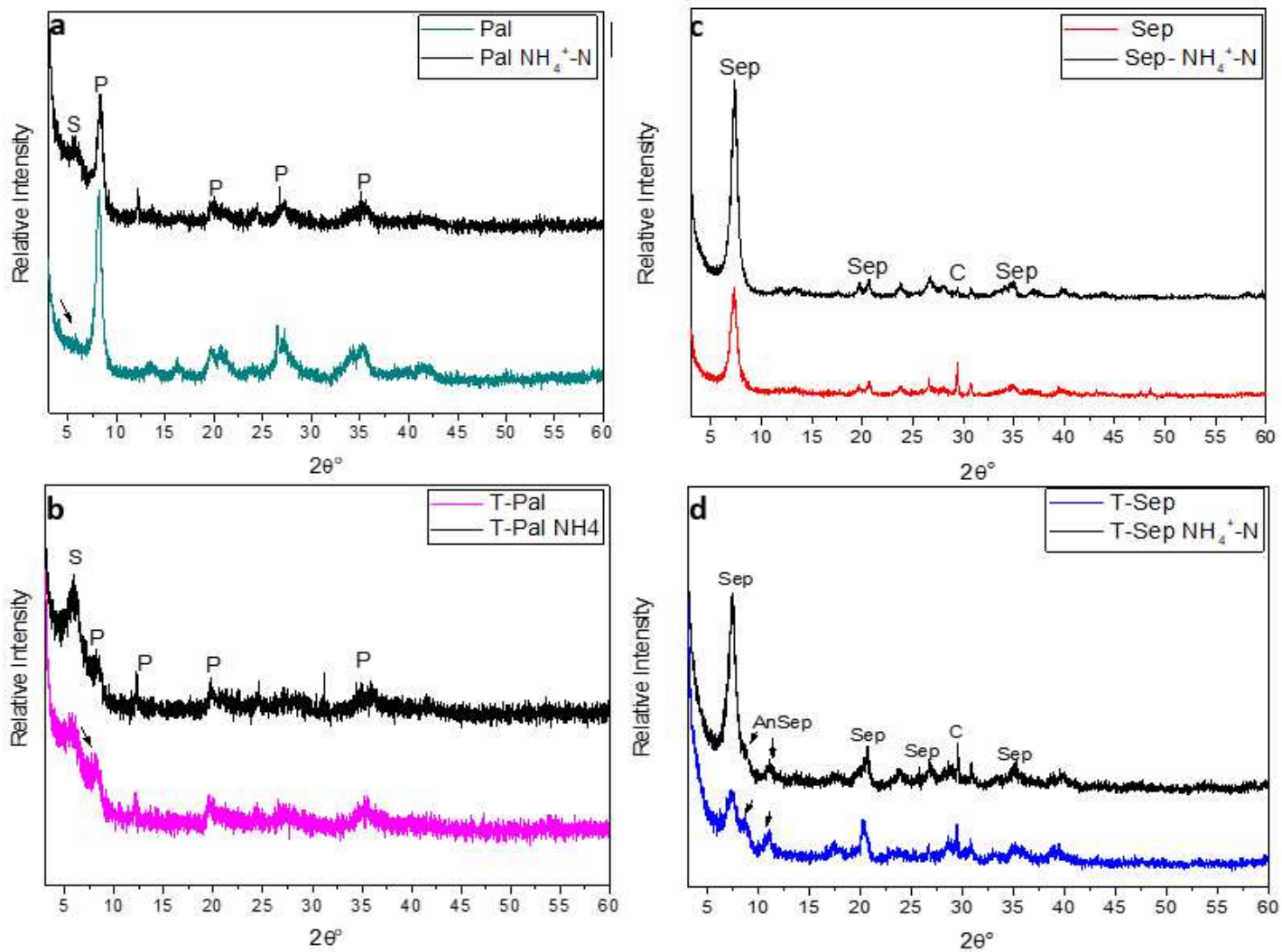


**Figure 1**

XRD patterns of a) Pal b) T -Pal c) Sep and d) T-Sep before and after  $\text{NH}_4^+\text{-N}$  adsorption where P: palygorskite, S: saponite, Sep: sepiolite, AnSep: sepiolite anhydrite and C: calcite.

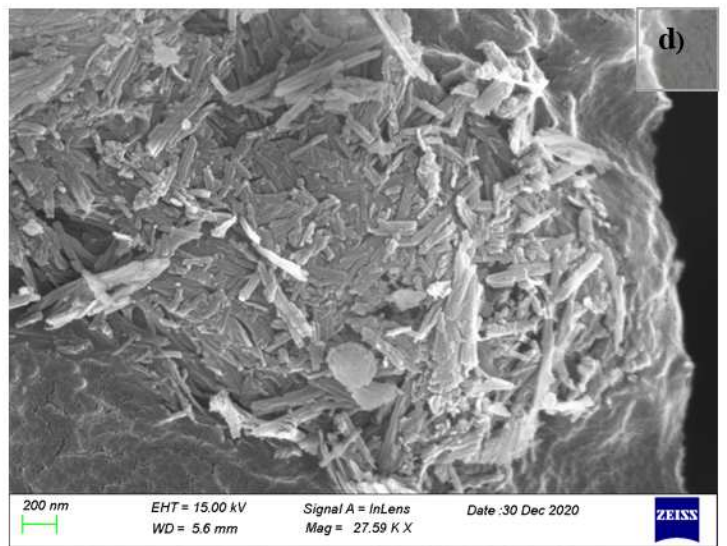
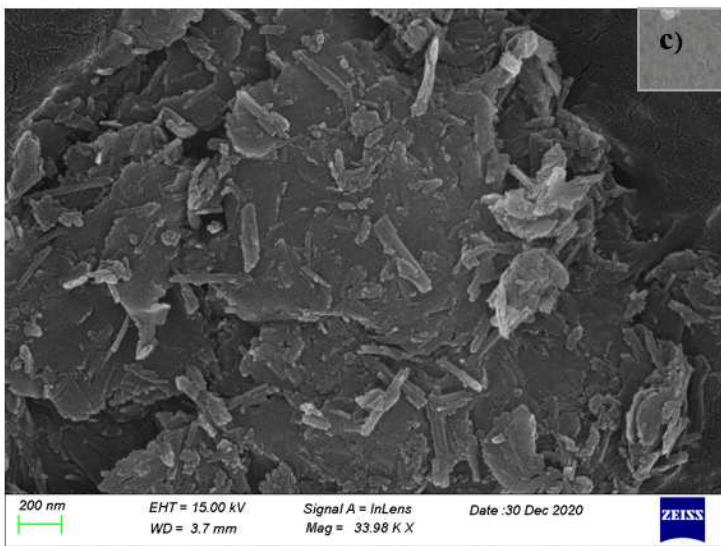
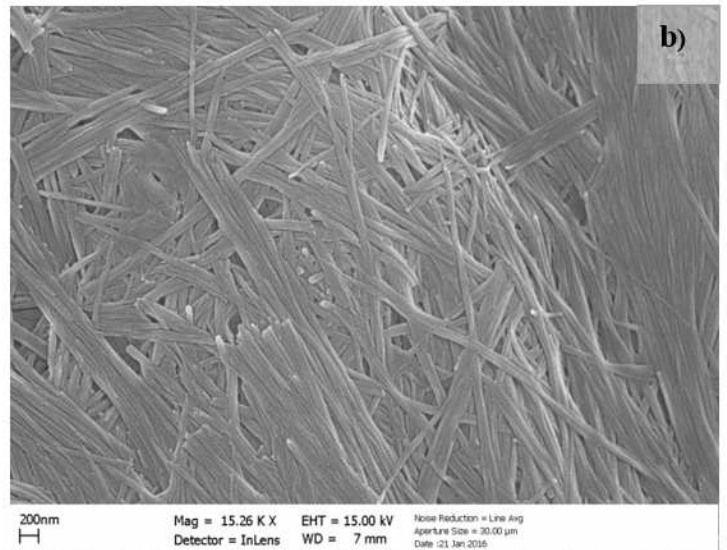
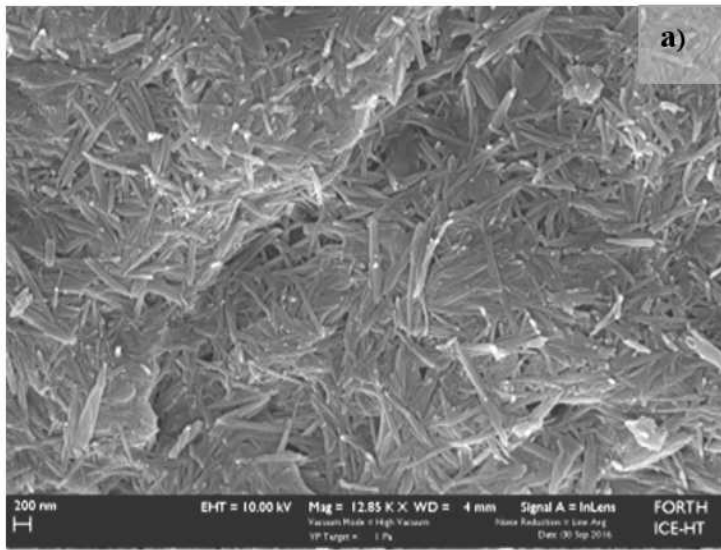


Figure 2

Scanning Electron Microscopy (SEM) images of a) Pal b) Sep c) T-Pal and d) T-Sep at 200 nm.

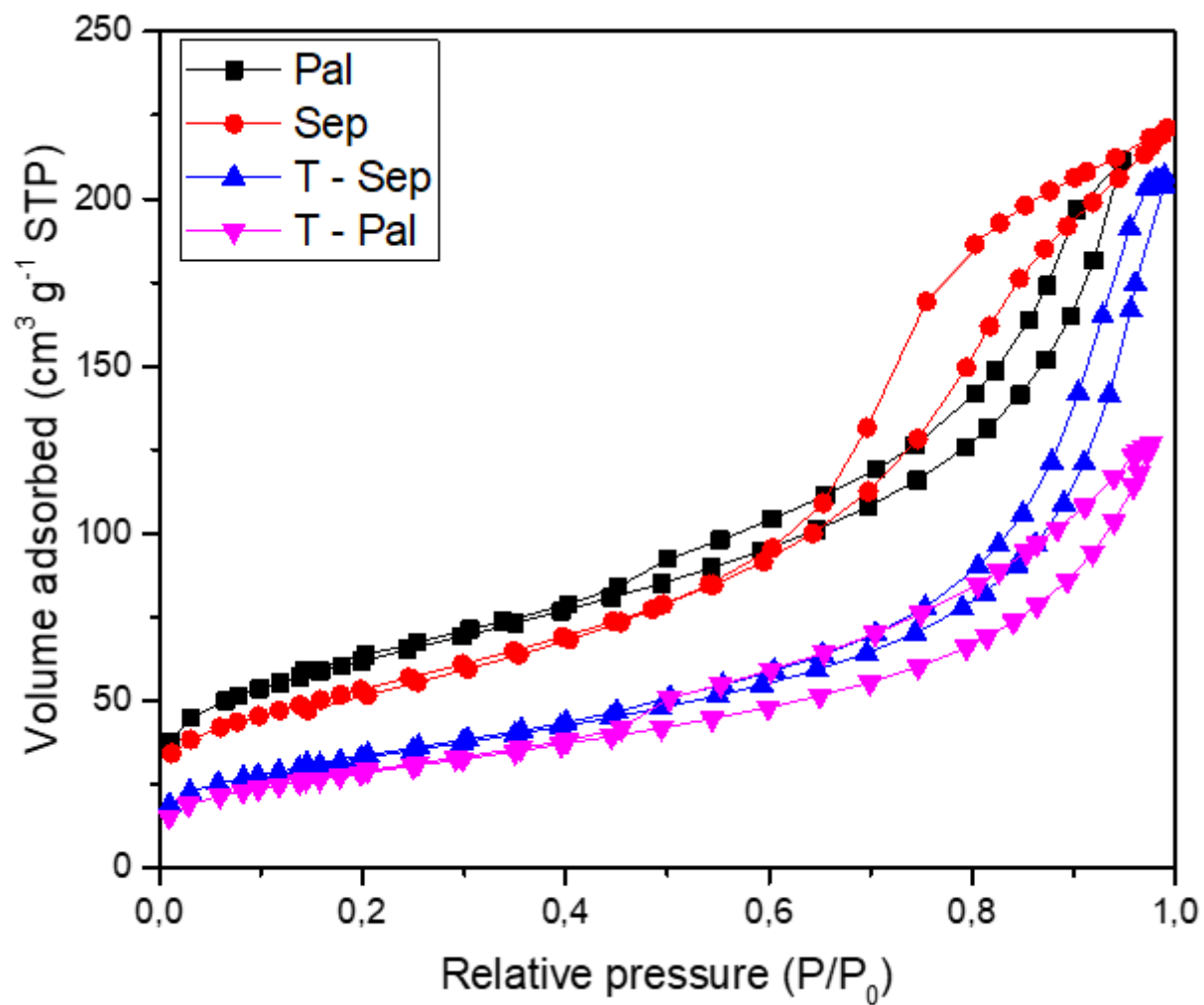


Figure 3

N<sub>2</sub> sorption – desorption isotherms plot from BET analysis for Pal, Sep, T-Pal and T-Sep.

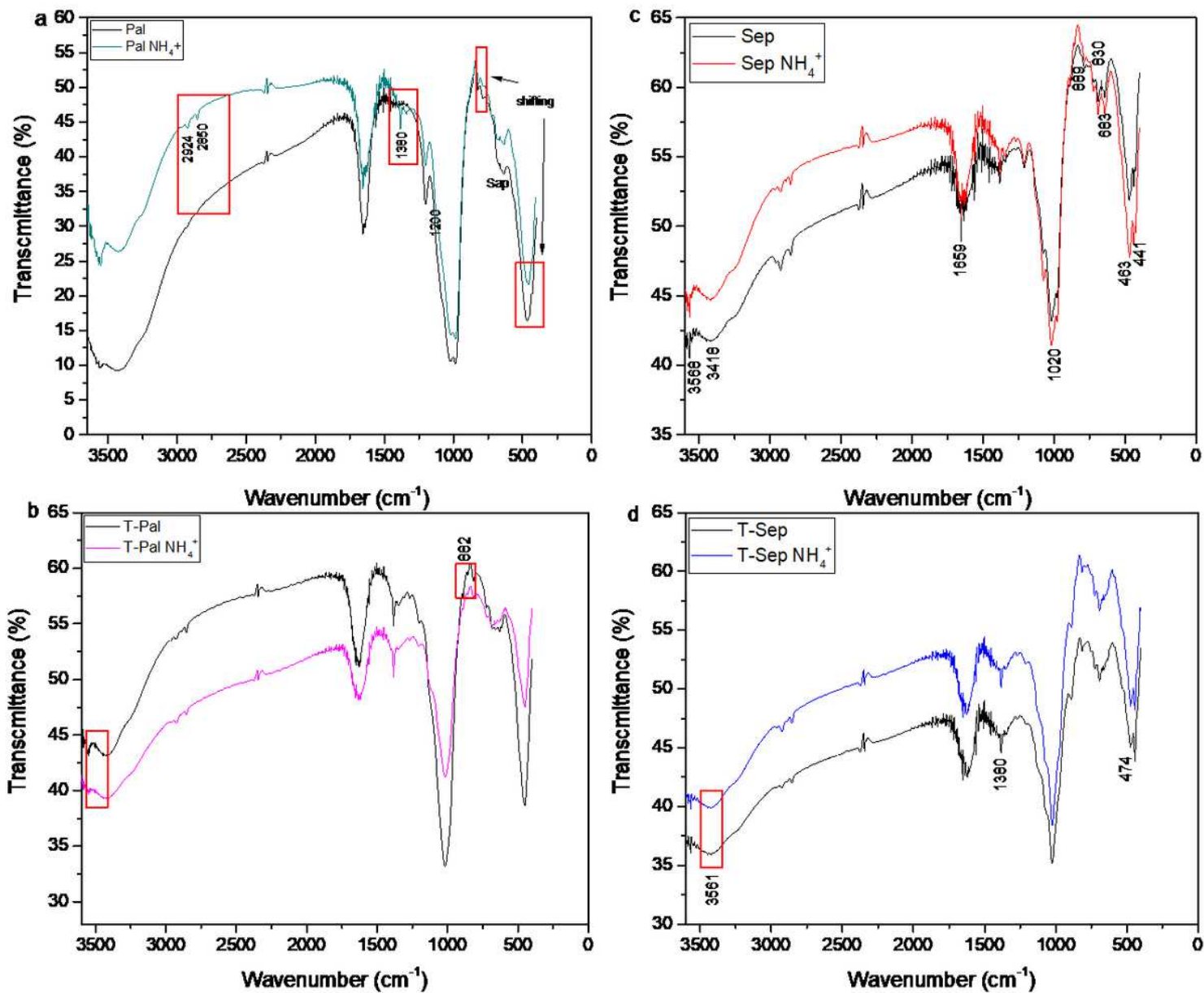


Figure 4

FT-IR spectra before and after  $\text{NH}_4^+$ -N adsorption of a) Pal b) T-Pal c) Sep and d) T-Sep.

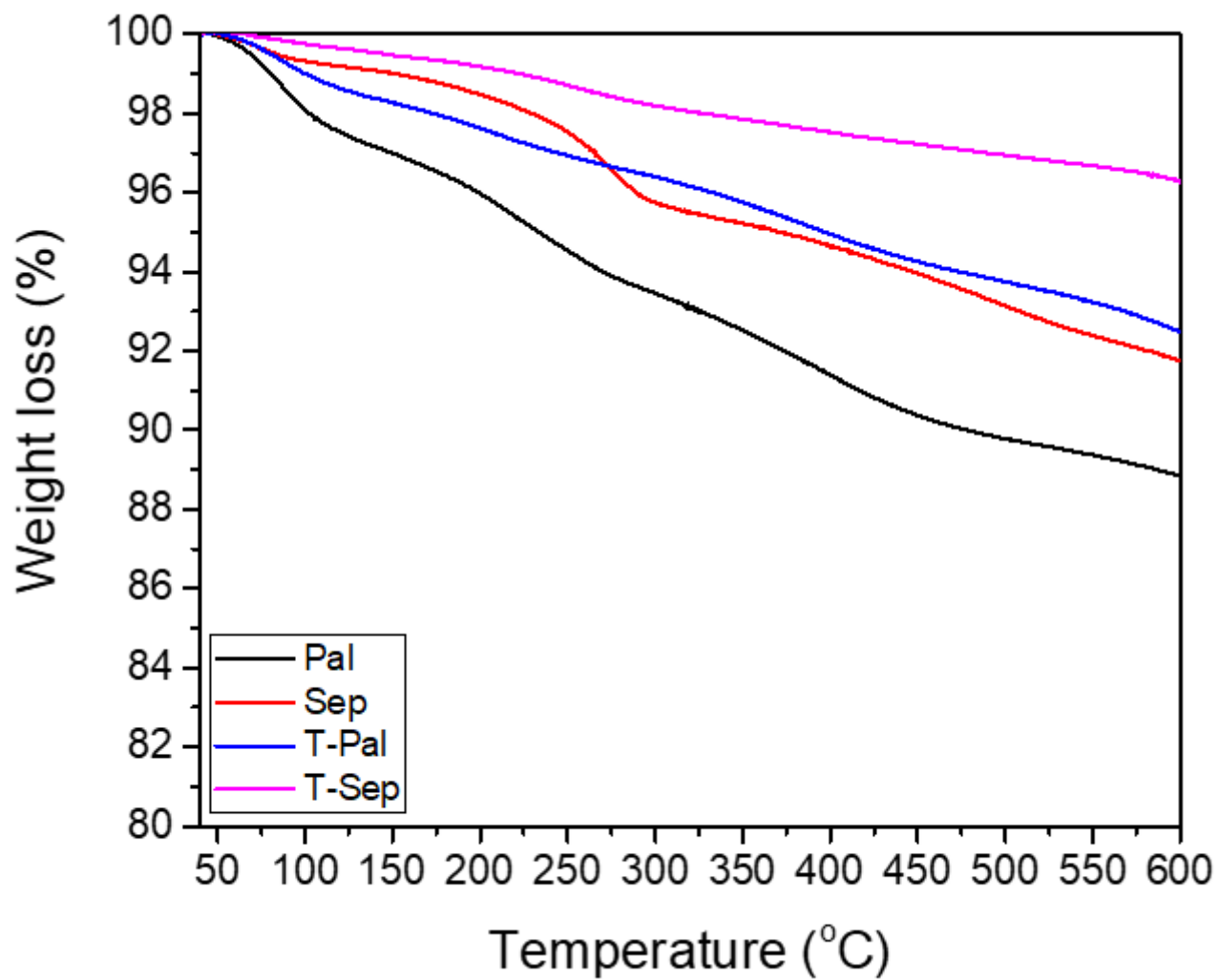


Figure 5

TGA curves of Pal, Sep, T-Pal and T-Sep.

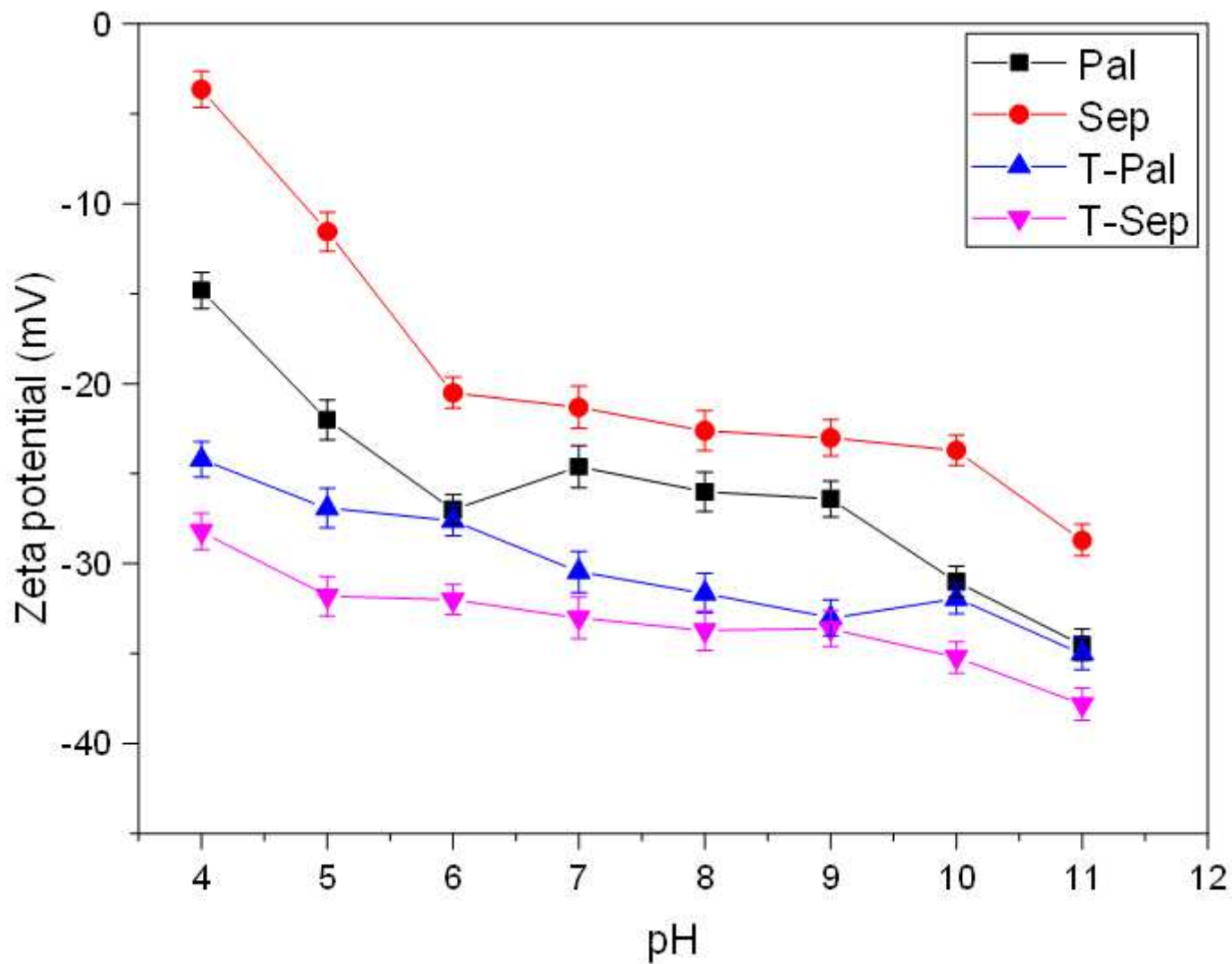
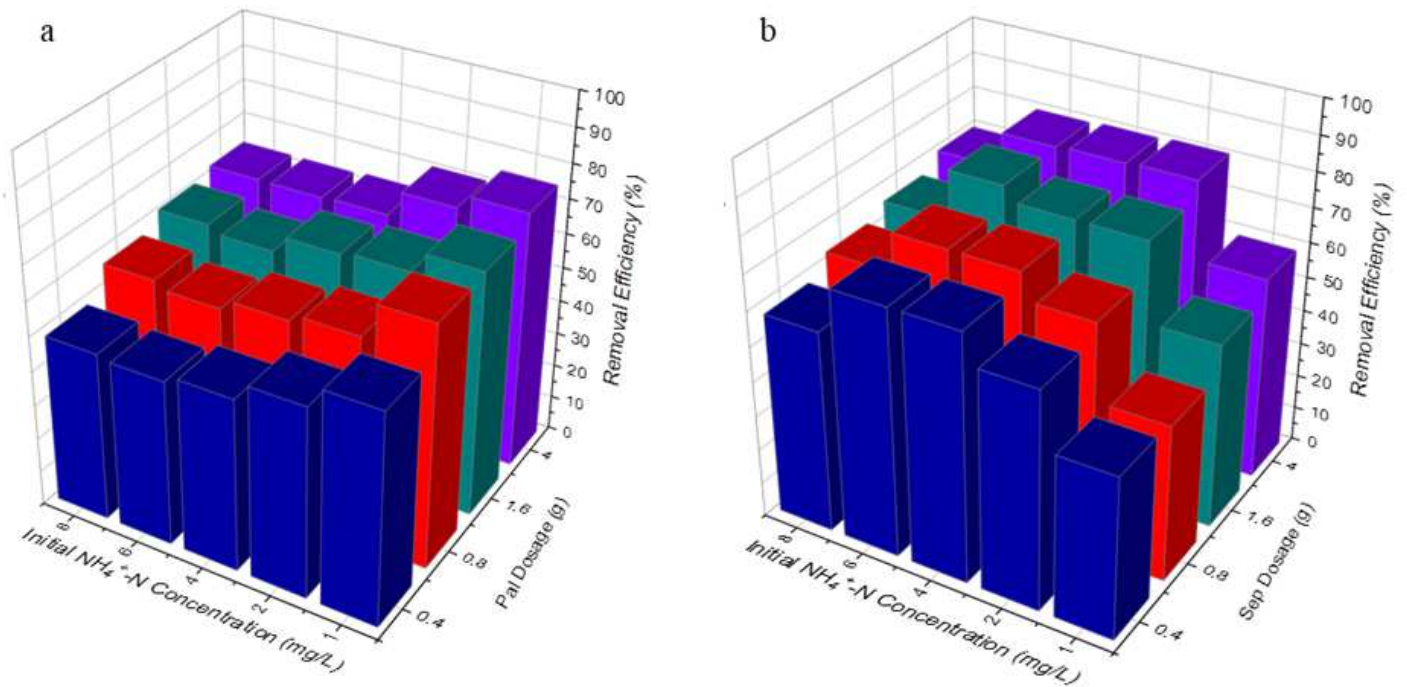


Figure 6

The zeta potential of Pal, Sep, T-Pal and T-Sep at pH range 4-11.



**Figure 7**

Maximum  $\text{NH}_4^+\text{-N}$  Removal Efficiency (%) with 0.4, 0.8, 1.6 and 4 g a) Pal and b) Sep for  $\text{NH}_4^+\text{-N}$  initial concentration 1, 2, 4, 6 and 8 mg/L. The removal efficiency (%) is the mean value from duplicate experiments.

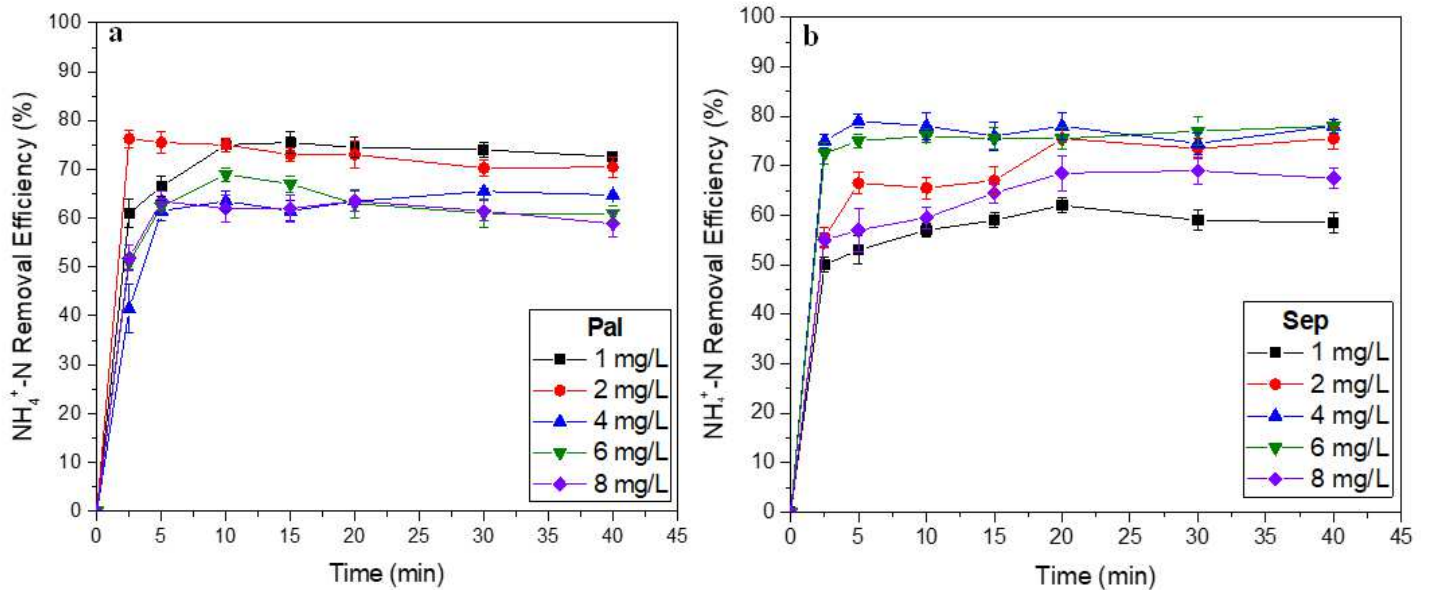


**Figure 8**

The effect of initial concentration on  $\text{NH}_4^+\text{-N}$  removal by 4 g a) Pal and b) Sep.

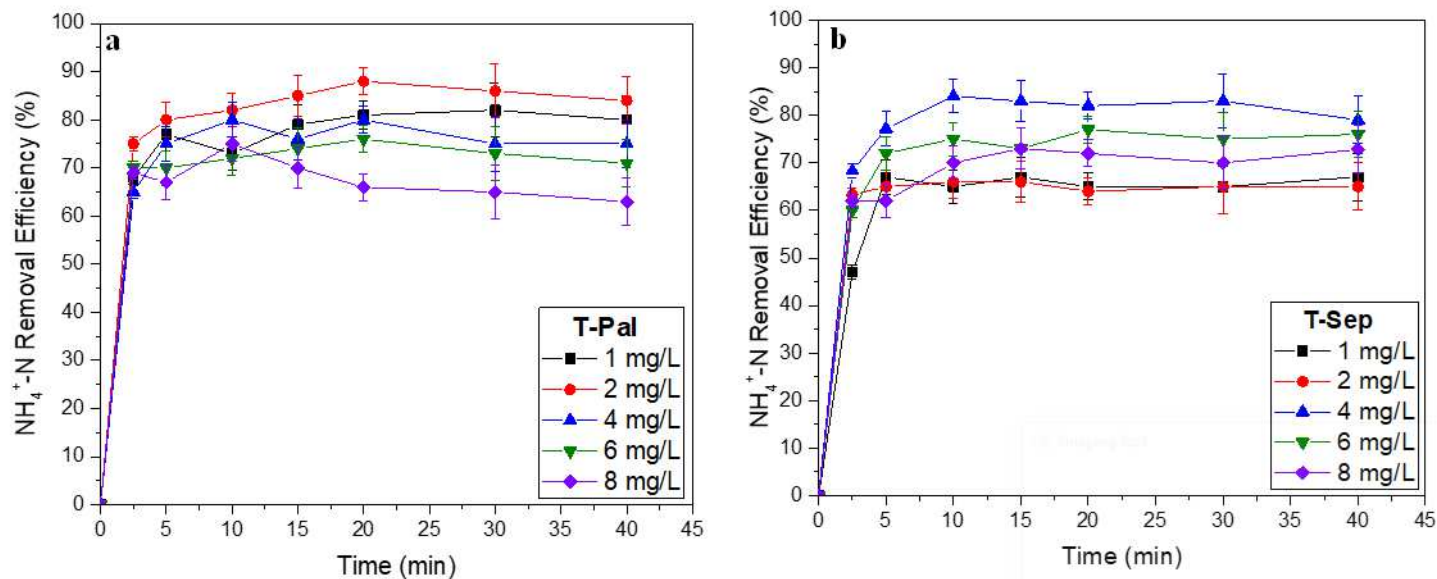


**Figure 9**

The effect of initial concentration on  $\text{NH}_4^+\text{-N}$  removal by 4 g a) T-Pal and b) T-Sep.

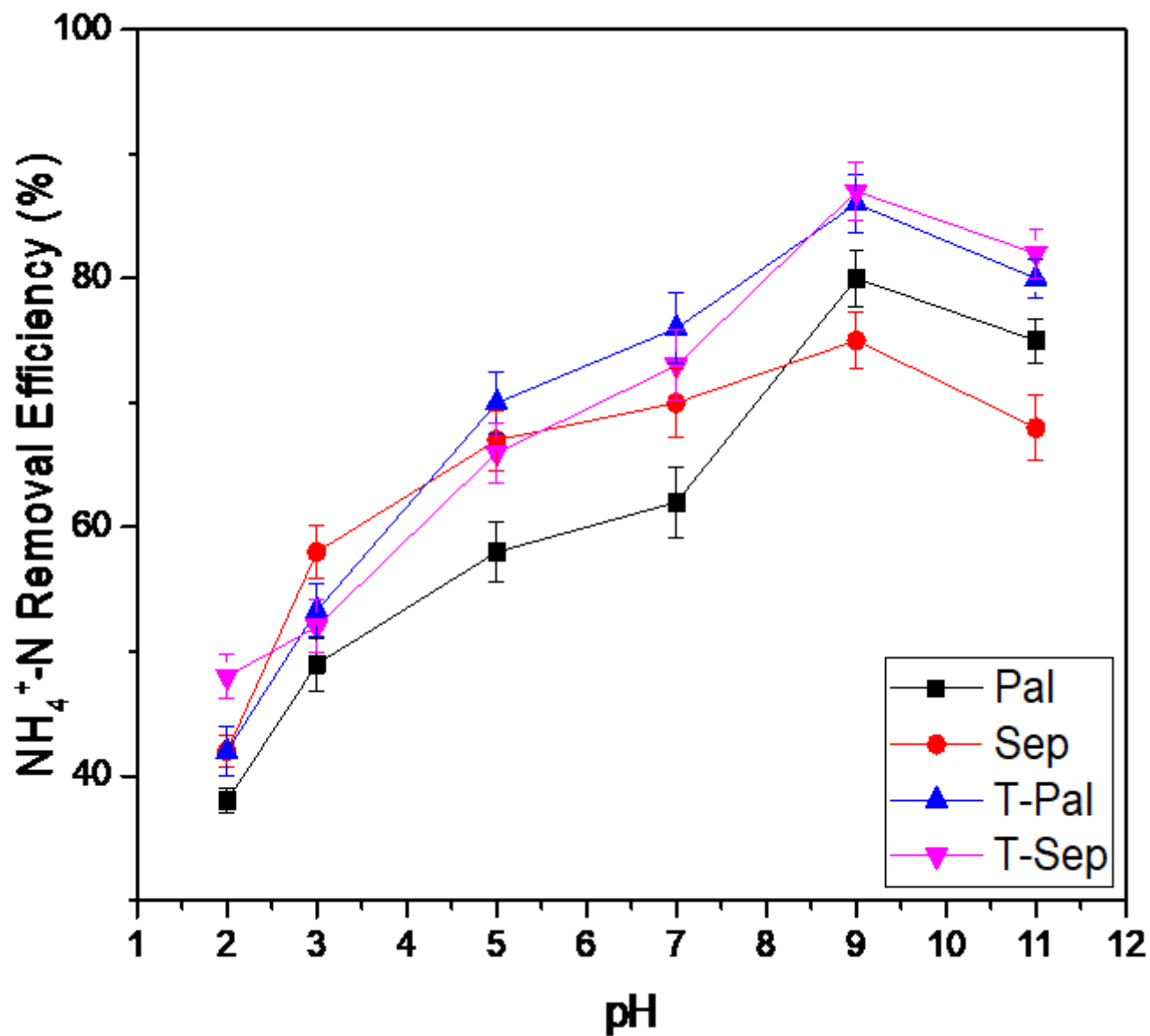


Figure 10

The effect of pH on NH<sub>4</sub><sup>+</sup>-N removal by 4 g Pal, Sep, T-Pal and T-Sep. (4 mg NH<sub>4</sub><sup>+</sup>-N /L, V= 200 ml, 20 min)

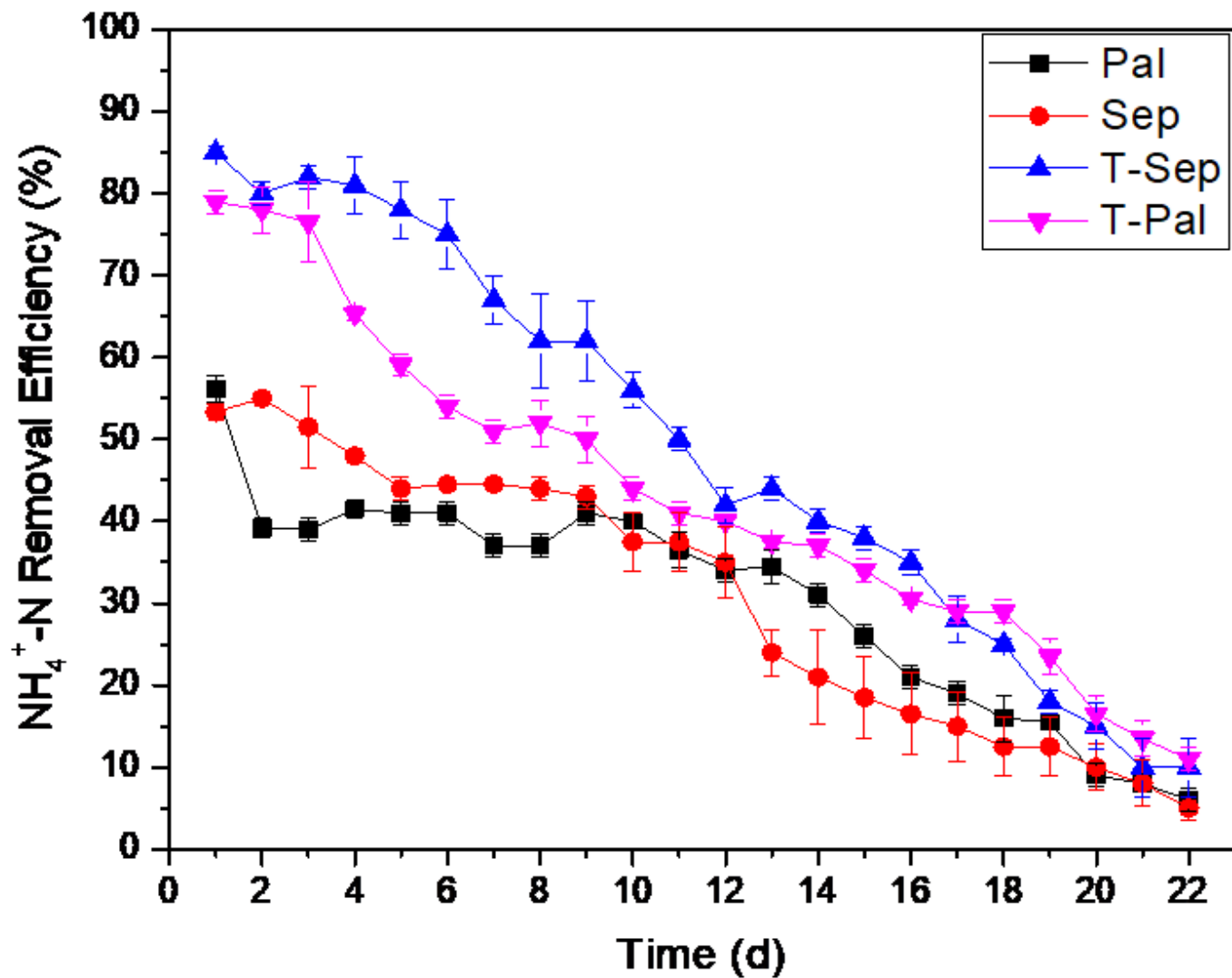


Figure 11

Saturation test of 4 g Pal, Sep, T-Pal and T-Sep in  $\text{NH}_4^+\text{-N}$  solution. (4 mg  $\text{NH}_4^+\text{-N}$  /L, V= 200 ml, pH= 5.5)

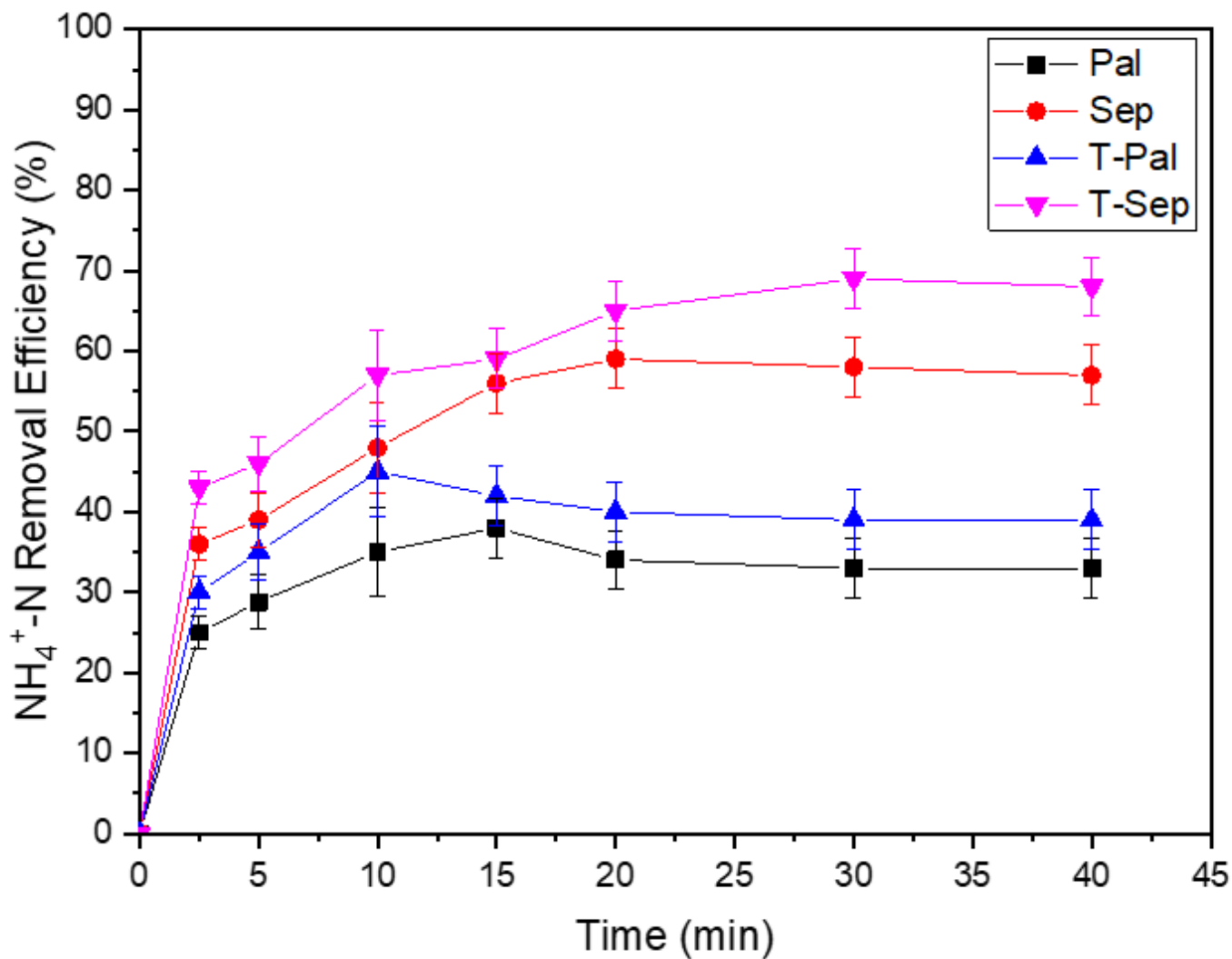


Figure 12

Removal efficiency (%) of 4 g Pal, Sep, T-Pal and T-Sep in real water sample contaminated with 4 mg/L  $\text{NH}_4^+\text{-N}$ .

## Supplementary Files

This is a list of supplementary files associated with this preprint. Click to download.

- [Graphicalabstract.png](#)